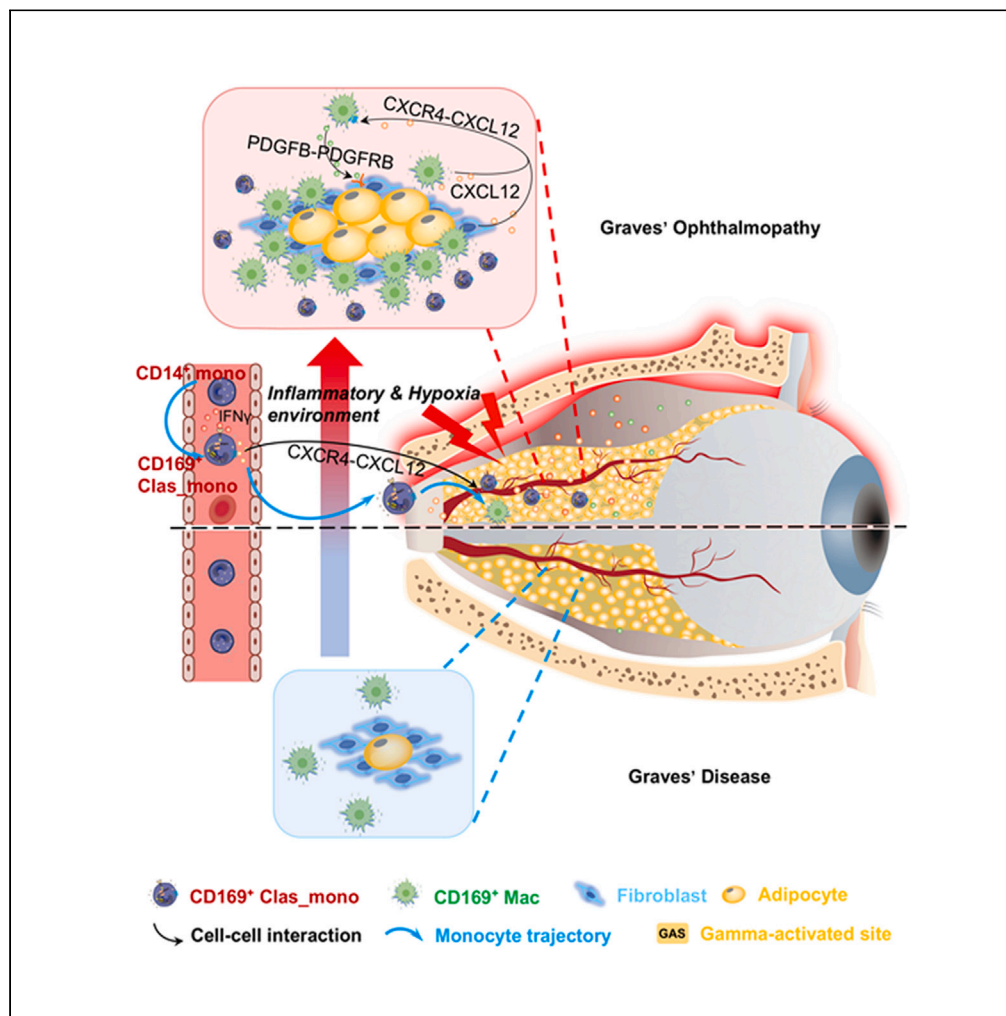Article

CD169⁺ classical monocyte as an important participant in Graves' ophthalmopathy through CXCL12-CXCR4 axis

Dongliang Wang,
Jie Ling,
RongQiang Tan,
..., Wuyou Gao,
Huijing Ye,
Xianchai Lin

yehuijing@qq.com (H.Y.)
linxch7@mail.sysu.edu.cn (X.L.)

Highlights

scRNA-seq of PBMCs identifies CD169⁺ clas_mono associated with GO progression

CD169⁺ clas_mono expansion is related to activated IFNγ signaling pathway in GOs

Circulating monocytes regulate GO development via Cxcl12-Cxcr4 axis

Article

CD169^{+} classical monocyte as an important participant in Graves' ophthalmopathy through CXCL12-CXCR4 axis

Dongliang Wang,[1,3] Jie Ling,[1,3] RongQiang Tan,[2,3] Huishi Wang,[1] Yixin Qu,[1] Xingyi Li,[1] Jinshan Lin,[1] Qikai Zhang,[1] Qiuling Hu,[1] Zhong Liu,[1] Zhaojing Lu,[1] Yuheng Lin,[1] Li Sun,[1] Dingqiao Wang,[1] Ming Zhou,[1] Zhuoxing Shi,[1] Wuyou Gao,[1] Huijing Ye,[1,*] and Xianchai Lin[1,4,*]

SUMMARY

Patients with Graves' disease (GD) can develop Graves' ophthalmopathy (GO), but the underlying pathological mechanisms driving this development remain unclear. In our study, which included patients with GD and GO, we utilized single-cell RNA sequencing (scRNA-seq) and multiplatform analyses to investigate CD169^{+} classical monocytes, which secrete proinflammatory cytokines and are expanded through activated interferon signaling. We found that CD169^{+} clas_mono was clinically significant in predicting GO progression and prognosis, and differentiated into CD169^{+} macrophages that promote inflammation, adipogenesis, and fibrosis. Our murine model of early-stage GO showed that CD169^{+} classical monocytes accumulated in orbital tissue via the Cxcl12-Cxcr4 axis. Further studies are needed to investigate whether targeting circulating monocytes and the Cxcl12-Cxcr4 axis could alleviate GO progression.

INTRODUCTION

Graves' disease is an autoimmune disorder that causes hyperthyroidism and eye symptoms due to autoantibodies targeting TSHR. Graves' ophthalmopathy (GO) is present in 25–50% of GD patients and is an indication that intervention early in the course of this systemic autoimmune condition holds promise for improved clinical outcomes.[1,2] However, our comprehension of GO pathophysiology remains limited. The development of GO is known to involve a complex interplay among cytokines, including the IFN-γ, CXCL8, and TNF-α, which ultimately leads to the infiltration of immune cells into orbital tissue, induction of fibroblast proliferation, and activation of orbital fibroblasts (OFs).[3–5] Although previous research has primarily focused on moderate to severe cases of GO,[6,7] important questions regarding how immune cell changes affect orbital inflammation and peripheral blood immunity remain unanswered.[3–5,8–10]

CD14^{+} monocytes are implicated in GO immune cell changes,[9,11] differentiating into macrophages or dendritic cells that can modulate immune responses and potentially worsen the disease. Previous studies have suggested high levels of TSHR and IGF-1R protein expression in both OFs and CD34^{+}CXCR4^{+}Col1^{+} monocyte-derived fibrocytes,[12,13] although further research is necessary to obtain a complete understanding of these changes.

GO treatment typically involves the use of glucocorticoids to reduce ocular inflammation; unfortunately, these agents sometimes have undesirable side effects.[1] Furthermore, newer therapies may be unsuitable for all patients.[14,15] Thus, there is a need for an accurate method to forecast treatment response and identify individuals who would benefit from various therapies. Indeed, developing such a marker to predict treatment response becomes essential in improving the effectiveness of treatments and reducing adverse effects.

In this study, we utilized scRNA-seq to identify transcriptional heterogeneity among monocytes and an expansion of CD169^{+} clas_mono in GOs. Our results showed that these cells, along with CD169^{+} clas_mono-derived macrophages, contributed to hyperinflammation, fibrosis, and adipogenesis in orbital tissues. Depletion of circulating monocytes prevented the progression of GO in mouse models and may serve as a potential therapeutic target and biomarker for assessing GO prognosis and severity. Our findings provide a comprehensive understanding of immune dysfunction in GO and offer additional insight into the development of more effective treatments for this autoimmune disorder.

A

B

C

D

E

F
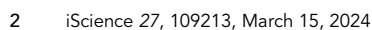
Figure 1. Single-cell transcriptomics of PBMCs identifying CD169⁺ classical monocytes associated with GO progression

(A) Workflow chart of the overall experimental design.

(B) Left, UMAP plot showing the distribution of different cell types in the peripheral blood from 5 GO patients and 4 GD patients. Right, UMAP plots showing expression of representative marker genes for the major cell types in PBMCs.

(C) Heatmap showing the distribution of upregulation DEGs in each cell type. Each column represents one cell type, and each row represents upregulated genes (LogFC >0.5, adjusted p value <0.05).

(D) Combined volcano plot showing up- and downregulated genes across the most effectively changed cell types in GOs (an adjusted p value <0.01 is indicated in red; an adjusted p value ≥0.01 is indicated in black; genes within IFN pathways and inflammation are labeled). Bar plot depicting enriched pathways of the significantly upregulated genes in combined volcano plot.

(E) UMAP visualization of monocytes from the transcriptomic atlas of PBMCs, colored by the identified monocyte subtypes. Boxplots comparing the differences in cell proportions between GOs (orange) and GDs (green) in the selected monocytes. The data are summarized as the mean ± SD. Statistical analysis was performed using Wilcoxon test. ns, not significant; *p < 0.05.

(F) Mass cytometry plot (Top) and bar plot (Bottom) showing the proportions of CD169⁺ classical monocytes in peripheral monocytes from GOs (n = 22) and GDs (n = 20). The data are summarized as the mean ± SD. Statistical analysis was performed using independent-sample t test. **p < 0.01.

RESULTS

Single-cell transcriptomics of PBMCs identifying CD169⁺ classical monocytes associated with GO progression

We performed a single-cell transcriptomic atlas of PBMCs from five GO patients (GOs) with Clinical Activity Score (CAS) ≤ 3 and four GDs using scRNA-seq (10x Genomics) technique (Figure 1A). To ensure high-quality data, we excluded cells with fewer than 200 unique molecular identifiers (UMIs) or more than 6000 UMIs, and cells containing over 10% of reads from mitochondrial genes (Figure S1A). After collecting a total of 62,096 high-quality cells, we corrected for batch effects, and used uniform manifold approximation and projection (UMAP) to identify 29 cell type clusters, including CD4T cells (CD4⁺), CD8T cells (CD8A⁺), B cells (MS4A1⁺), natural killer (NK) cells (NCAM1⁺), classical monocytes (Clas_mono, CD14⁺ FCGR3A⁻), non-classical monocytes (Nonclas_mono, FCGR3A⁺), plasmacytoid dendritic cells (pDCs; LILRA4⁺), and conventional dendritic cells (cDCs; CD1C⁺) (Figures 1B, S1B, and S1C). Our analysis revealed sixteen T cell subtypes (CD4T_0–4, CD8T_0–7, proT, γδT and DNT), four B cell subtypes (B_0–4), three NK cell subtypes (NK_0–2), five myeloid cell subtypes (Clas_mono, Inter_mono, Nonclas_mono, pDCs and cDCs) and Fibrocyte-like cells (Fibrocyte-like), based on the expression of canonical markers and unique marker genes (Figure S1E).[16,17] We found that cells from multiple GO patients were present in each cluster, indicating the effectiveness of our batch correction method (Figures S1B, S1C, and S1D).

Comparing transcriptomic profile of PBMCs from GO and GD, we identified hundreds of DEGs between GOs and GDs to understand the molecular events involved in the development of GO. Our DEGs analysis revealed significant alterations in clas_mono during GO (Figures 1C, S1F, and S1G). Further enrichment analysis of DEGs in these cell types (Figures 1D, S1J, and S1H) revealed that monocytes expressed increased levels of interferon-related genes and inflammation-related genes (Figure 1D). Also, our study found that Fibrocyte-like cells (Figure S1I) exhibited increased expression of lymphoid lineage development and cell activation-related genes,[18–20] while clas_mono (Figure S1I) displayed increased expression of genes involved in mononuclear cell migration, blood vessel development and the inflammatory response (Figure S1J). Conversely, downregulated DEGs in clas_monos were enriched in protein ubiquitination regulation and negative regulation of phosphate metabolism (Figure S1H). These changes in gene expression might hinder the degradation of phosphorylated-STAT1, leading to increased proinflammatory and interferon signaling and contributing to GO development.[21] By capturing the significant contribution of monocytes to the global transcriptome aberrations in PBMCs during GO, we reason that monocytes may be an important participant in GO progression.

Next, single-cell transcriptomic analysis of peripheral blood monocytes detected potential pathogenic mechanisms through which various subtypes could impact GO development. We clustered the profiles of these monocytes using a graph-based method, resulting in the identification of eight distinct subpopulations: (1) CD16⁻ CD14⁺ classical monocytes (Mono_0; CD16⁻CD14⁺); (2) major histocompatibility complex (MHC)-II-high monocytes (Mono_1; CD16⁻CD14⁺HLA-DRA⁺HLA-DQB1⁺); (3) VIM-high monocytes (Mono_2; CD16⁻CD14⁺VIM⁺PADI4⁺); (4) CD16⁺CD14⁻ nonclassical monocytes (Mono_3; CD16⁺CD14⁻); (5) CD169⁺ classical monocytes (Mono_4, CD169⁺ clas_mono; CD16⁻CD14⁺CD169⁺); (6) GNLY-high monocytes (Mono_5; CD16⁻CD14⁺GNLY⁺); (7) CD69-high monocytes (Mono_6; CD16⁻CD14⁺CD69⁺) and (8) unknown monocytes (Mono_7). These subpopulations were not influenced by individual patients or conditions (Figures 1E and S2A). We further assessed the functional phenotypes of these monocyte subtypes by evaluating the highly expressed genes and corresponding enriched pathways (Figure S2A). The results showed that VIM-high monocytes (Mono_2) expressed high levels of the PADI4 gene, associated with HIF-1α expression and vascularization.[22] The CD169⁺ clas_mono (Mono_4) displayed high expression of IFN-inducible genes (ISG15, SIGLEC1, IFIT2 and CXCL10) and classical monocyte markers (CD14⁺CD16⁻).[11,17] The CD16⁻ CD14⁺ classical monocytes (Mono_0) were similar to VIM-high cells but not enriched in neutrophil degranulation. CD16⁺ CD14⁻ monocytes (Mono_3) showed markers of nonclassical monocytes (FCGR3A, C1QA). MHC-II-high monocytes (Mono_1) were enriched in genes involved in antigen presentation pathways, such as those encoding MHC class II chains (HLA-DRA, HLA-DQB1, HLA-DPA1 and HLA-DPB1). GNLY-high monocytes (Mono_5) had high expression of components of GNLY and IL32, which promotes monocyte differentiation into macrophage-like cells.[23] Finally, CD69-high monocytes (Mono_6) were highly enriched in genes involved in the positive regulation of immune response.[24] We analyzed the difference in monocyte composition in patients with GO. Our comparison between GO and GD patients revealed a significant increase in the population of CD169⁺ clas_mono in GO patients (Figure 1E). Mass cytometry confirmed this increase (Figures 1F and S2F). Our gene expression analysis showed that the CD169⁺ clas_monos were enriched in cytokines secretion, migration, and phagocytosis-related genes (Figure S2D), including CCL8, CCL2, GSDMD, ATF5 and RELB (Figure S2E). These genes play a role in inflammation, pyroptosis,[25] adipogenesis[26] and cell activation.

In summary, our analysis of monocyte subtypes from PBMCs indicated the diversity of circulating monocytes and their varied duties, as well as a significant enhancement of the CD169^{+} clas_mono in GO patients.

Peripheral CD169^{+} clas_mono exhibits pro-inflammation characteristics

To evaluate the proinflammatory properties of CD169^{+} clas_mono, we assessed three aspects of their inflammation-regulatory abilities: secretion of ocular inflammation-specific cytokines, phagocytosis, and migration. The results showed that CD169^{+} class monocytes had higher functional capabilities compared to other subsets (Figure 2A), as demonstrated by their overexpression of proinflammatory cytokines associated with ocular inflammation, including *CXCL10, CXCL8, CCL3, CCL4, CCL2, TNF* and *IL6* (Figure S2B).[5,8,27,28]

Next, we evaluated the phagocytic capacity of CD169^{+} clas_mono by incubating them with fluorescence-labeled dextran. Flow cytometry analysis results revealed that CD169^{+} clas_mono from GOs engulfed more dextran than CD169^{+} clas_mono from GDs (Figure 2B). Using a Transwell assay, we found that the migration of CD169^{+} clas_mono toward the chemokine CCL2 was also increased in GOs (Figure 2C). Additionally, we analyzed the production of proinflammatory cytokines in response to lipopolysaccharide (LPS) stimulation in CD169^{+} clas_mono. The results showed that the CD169^{+} clas_mono subpopulation derived from GOs produced significantly higher levels of TNF-α and IL6 compared with GDs (Figure 2D). Meanwhile, we identified potential transitional relationships among monocyte subtypes through Monocle2 algorithm (Figures S3A and S3B). Pseudo-time trajectory analysis suggests that in patients with GO, the differentiation of monocytes toward a CD169^{+} clas_mono pathway was favored and was accompanied by inflammation (Figures S3A, S3B, and S3C). Overall, both our experimental validations and bioinformatics analyses indicate that CD169+ clas_mono possesses proinflammatory properties related to GOs.

Peripheral CD169^{+} clas_mono expansion is related to high levels of interferons in GO

To analyze the regulatory networks involved in GO, we used the pySCENIC[29] tool to identify the most critical transcription factors (TFs) regulating the DEGs across seven monocyte subclusters (Figure 3A). Our results showed that TFs disrupted in GO were mainly located in the CD169^{+} clas_mono, Mono_0, and Mono_2 subclusters (Figure 3A). Among the TFs, *IRF7, STAT2, STAT1, CEBPD, IRF1, CEBPB, SPI1,* and *JUN* were the most important. The DEGs modulated by *STAT1, STAT2,* and *IRF7* in these monocyte clusters were significantly enriched in interferon signaling, chemokine receptors binding chemokines, and antigen processing and presentation (Figure 3A), as indicated by Metascape[30] analysis. Additionally, expression and activity of these TFs were enriched in CD169^{+} clas_mono from GOs (Figure S4A), and STAT1 phosphorylation was found to be significantly increased in CD169^{+} clas_mono derived from GOs (Figure 3B).

The observed enrichment of IFN-related pathways in CD169^{+} clas_mono prompted us to investigate the effect of interferons (IFNs) on these cells. We found that treatment with IFN-γ significantly increased the expression of CD169 genes in GD monocytes (Figure 3C) and elevated the proportion of CD169^{+} monocytes, with a greater effect compared to treatment with IFN-α or IFN-β (Figure 3D).

Furthermore, we observed significantly elevated levels of IFN-γ in the serum of patients with GO compared to GDs (Figure S4B). Previous studies have shown that CD4^{+} T lymphocytes, CD8^{+} T lymphocytes, and NK cells are the exclusive producers of IFN-γ.[31–34] To understand the interaction between CD169^{+} clas_mono and IFN-γ-producing cells, we conducted a CellChat analysis (Figure S4C and S4D).[35] Our findings revealed increased incoming interactions from NK/T cells to CD169^{+} clas_mono, particularly from CD4^{+} T cells in GO patients, indicating that elevated IFN-γ production by CD4^{+} T cells had a significant impact on CD169^{+} clas_mono. Furthermore, increased outgoing interactions from CD169^{+} clas_mono to CD4^{+} T cells suggested that CD169^{+} clas_monos in GO patients were sending intense signaling pathways. Pro-inflammatory interactions were also observed, including CD40LG-ITGAM_ITGB2,[36] LGALS9-CD44,[37,38] MIF-CD74_CD44[39,40] and BTLA-TNFRSF14 (Figure S4D).[41,42] These results demonstrated frequent crosstalk between CD169^{+} clas_mono and CD4^{+} T cells, the main IFN-γ–producing cells, in GOs, leading to increased expression of *CD169* genes. Further comprehensive analysis revealed that CD169^{+} class_mono in GO shared a similar transcriptomic pattern with CD169^{+} class_mono in other IFN-related autoimmune diseases, such as Vogt-Koyanagi-Harada (VKH), systemic lupus erythematosus (SLE), and rheumatoid arthritis (RA) (Figure S4E).[17,43–45] Our data suggested that IFN-γ was important in promoting the expansion of CD169^{+} clas_mono in GO.

Characterization of CD169^{+} macrophages in orbital tissues of GOs

Through immunofluorescence, we observed increased numbers of CD169^{+} clas_mono in GOs compared to GDs in orbital tissues (Figure 4A). To detect the characteristics of mononuclear phagocytes in orbital tissues of GOs, we re-clustered mononuclear phagocytes from single-cell orbital tissue atlas into four groups: CD169^{+} classical monocytes (CD169^{+} clas_mono; *CD14^{+}, CD169^{+}*), CD169^{-} macrophages (CD169^{-} Mac; *MARCO^{+}* and *CD169* low expression), CD169^{+} macrophages (CD169^{+} Mac; *MARCO^{+}* and *CD169* high expression) and dendritic cells (DCs; *CD1C^{+}*) (Figure 4B). Comparing the relative cell proportions in the GOs and GDs, we observed an increase in CD169^{+} Mac and CD169^{-} Mac in GOs and a decrease in DCs (Figure 4B). As previously established, the recruitment and infiltration of macrophages played a fundamental role in regulating inflammation and fibrosis in many physiological and pathological contexts.[46] Our results demonstrated that CD169^{+} macrophages exhibited higher scores for inflammation, pro-fibrosis and adipogenesis, indicating their importance in modulating exaggerated inflammation, adipogenesis and fibrosis in the orbital tissues of patients with GO (Figure 4C). *In vivo*, we incorporated images from immunofluorescence experiments that depict the co-localization of CD169^{+} macrophages with factors related to inflammation, fibrosis and adipogenesis (Figure 4D). *In vitro*, we cultured CD169^{+} macrophages isolated from the orbital tissues of GD and GOs. ELISA analysis of the culture supernatants revealed elevated levels of IL6, TGFB, and APOE (Figure S5B), indicating that CD169^{+} macrophages from GO patients possess inflammatory, pro-fibrotic, and adipogenic properties. To further validate the impact of these macrophages on OFs, we conducted additional co-culture experiments. After 48 h of co-culturing CD169^{+} macrophages with OFs, immunofluorescence staining analysis revealed
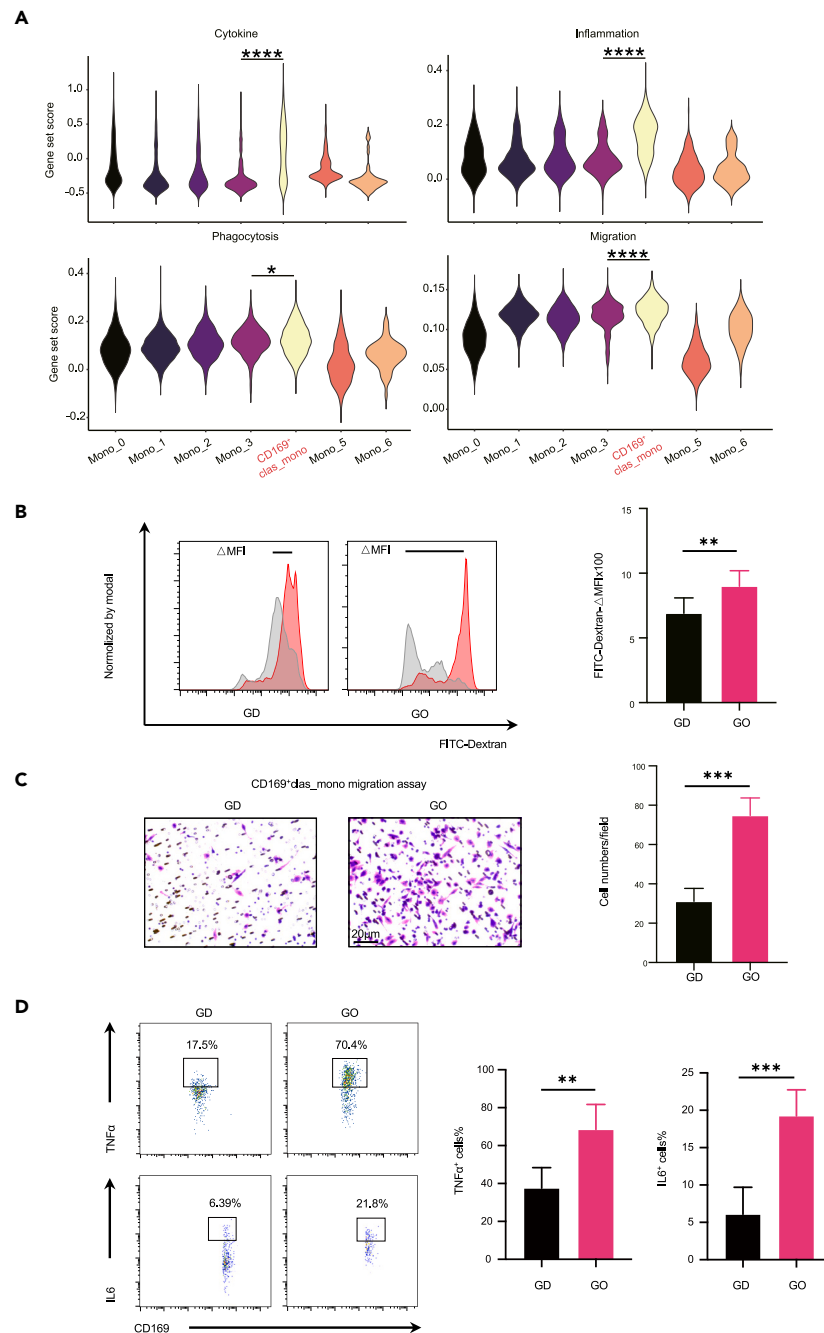
Figure 2. Peripheral CD169⁺ clas_mono exhibits pro-inflammation characteristics

(A) Violin plots displaying the average expression levels of inflammation-related functional gene sets among all monocyte subtypes (colors). Statistical analysis was performed using Wilcoxon test. *p < 0.05; ****p < 0.0001.

(B) Representative histograms and quantitative analysis of the phagocytosis capability of CD169⁺ clas_mono from GOs (n = 5) and GDs (n = 5). The data are summarized as the mean ± SD. Statistical analysis was performed using independent-sample t test. **p < 0.01.

(C) Representative histograms and quantitative analysis of monocytes migration capability of CD169⁺ clas_mono from GOs (n = 8) and GDs (n = 8). The data are summarized as the mean ± SD. Statistical analysis was performed using independent-sample t test. ***p < 0.001.

(D) Representative flow cytometry analysis and histograms showing the significantly higher production of IL6 (n = 6 in GOs and n = 6 in GDs) and TNFα (n = 6 in GOs and n = 6 in GDs) in CD169⁺ clas_mono from GOs after LPS stimulation. Statistical analysis was performed using independent-sample t test. All data with error bars are presented as mean ± SD. **p < 0.01; ***p < 0.001.
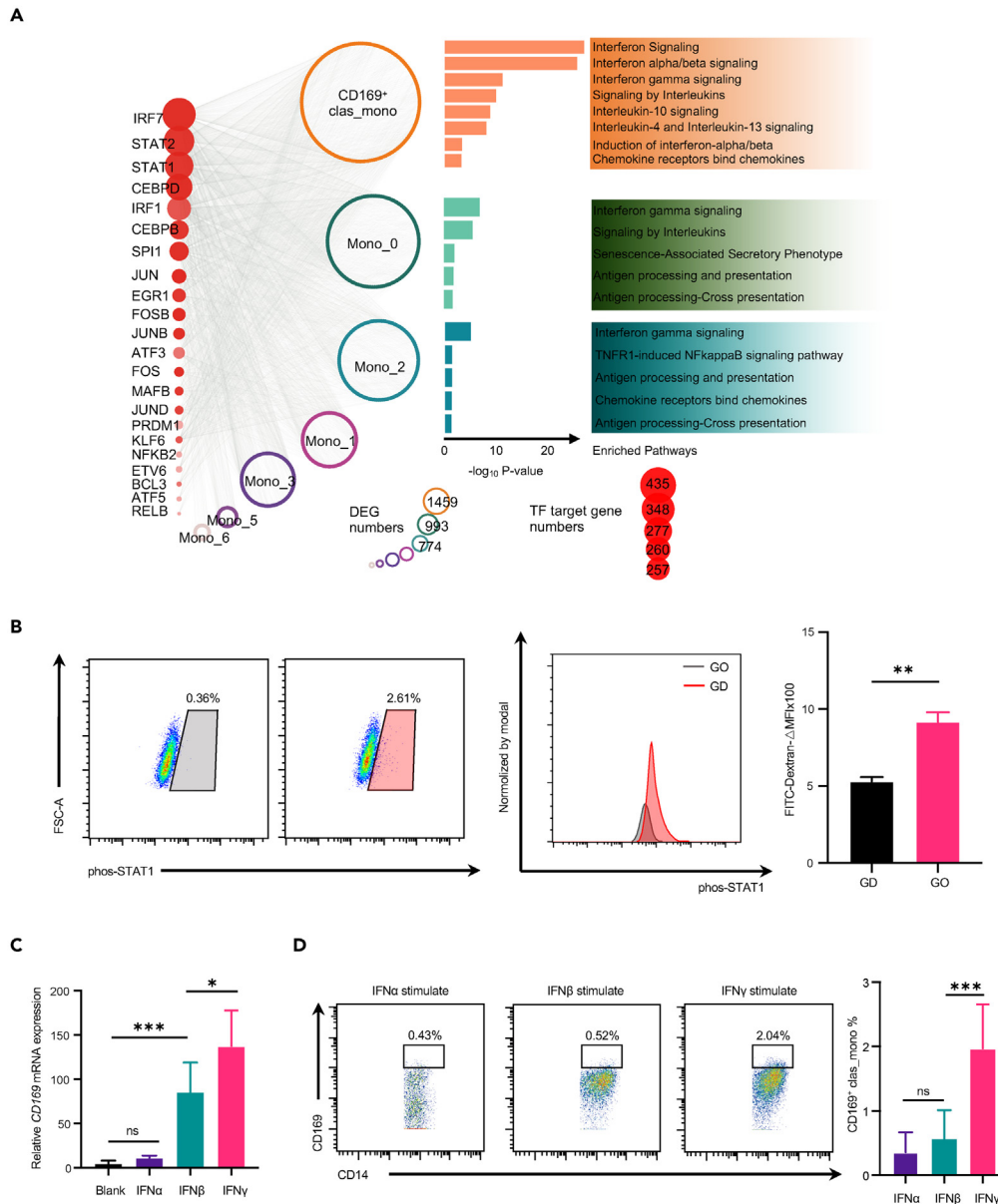
Figure 3. CD169+ clas_mono expansion is related to high levels of interferons in GO

(A) Network visualization of upregulated TFs and their target genes. The internal nodes annotate TFs; the circular edge denotes the downstream target upregulated DEGs of these TFs; bar plots showing the pathway enrichment of these DEGs. The node sizes are positively correlated to the number of associated DEGs.

(B) Representative histograms and quantitative analysis of phosphorylated STAT1 levels (normalized MFI values) in CD169+ clas_mono from the GO and GD groups (n = 6 per group). The data are summarized as the mean ± SD. Statistical analysis was performed using independent-sample t test. **p < 0.01.

(C) Monocytes were stimulated with IFN-γ, IFN-α and IFN-β for 6 h, and relative mRNA expression (*CD169* genes) was measured using qRT-PCR (n = 6). The data are summarized as the mean ± SD. Statistical analysis was performed using one-way ANOVA. ns, not significant; *p < 0.05; ***p < 0.001.

(D) Representative histograms and quantitative of the mass cytometry analysis results showing the proportions of CD169+ clas_mono after 24 h of IFN-γ, IFN-α and IFN-β stimulation (n = 6). Statistical analysis was performed using one-way ANOVA. All data with error bars are presented as mean ± SD. ns, not significant; ***p < 0.001.

significantly higher levels of fibrotic markers (α-SMA/FN1) in OFs from GO group compared to GD group (Figure 4E). Moreover, Oil Red O staining analysis revealed enhanced lipid accumulation in the GO group, highlighting the pro-adipogenic influence of CD169+ macrophages on OFs (Figure 4E). Collectively, these co-culture experiments combined with immunofluorescence and Oil Red O staining analyses, suggest that CD169+ macrophages from GO contribute to the activation of OFs and subsequent pathological changes.

A

B

C

D

E
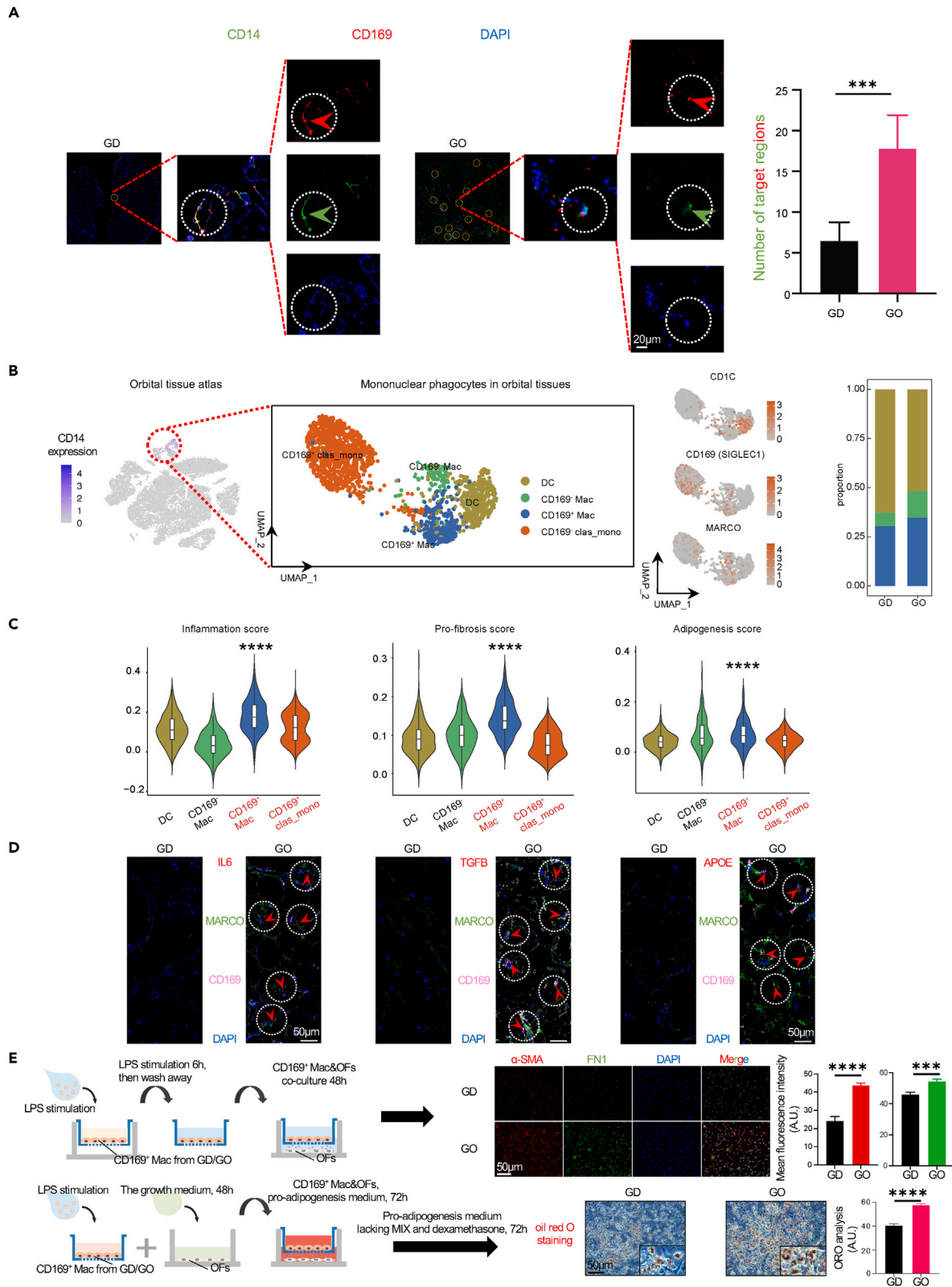
Figure 4. Characterization of CD169⁺ macrophages in orbital tissues of GOs

(A) Immunofluorescence staining demonstrating the distribution of Cd169⁺ clas_mono in orbital tissues from GDs and GOs. Histograms depicting the number of target regions within orbital tissues in GDs (n = 6) and GOs (n = 6). Target regions labeled by red or green arrows and white dashed lines. The data are summarized as the mean ± SD. Statistical analysis was performed using independent-sample t test. ***p < 0.001.

(B) Left, UMAP visualization of mononuclear phagocytes in orbital tissues. Middle, UMAP plots showing the expression of representative marker genes for the major cell types. Right, composition of the ratios of mononuclear phagocytes from orbital tissues in GOs and GDs.

(C) Violin plots displaying the average expression levels of functional gene sets among mononuclear phagocytes. Statistical analysis was performed using Wilcoxon test. ****p < 0.0001.

(D) IF staining demonstrating the co-localization of inflammatory, pro-fibrotic and adipogenic factors and CD169⁺ macrophages in orbital tissues from GOs. Target regions labeled by red arrows and white dashed lines.

(E) Diagram shows the CD169⁺ macrophages/OFs co-culture experiment. Visualization and quantification of fibrosis by IF staining analysis. IF staining of OFs showing α-SMA (red), FN1 (green), and DAPI (blue) after co-culture. Visualization and quantification of lipid accumulation by Oil red O (ORO) staining analysis. Insets from images are magnified five times. A.U., arbitrary units. All data with error bars are presented as mean ± SD. Statistical analysis was performed using independent-sample t test. ***p < 0.001; ****p < 0.0001.

We explored the functional changes of the four cell types in GO by conducting DEGs and Metascape analyses. Results showed that CD169⁺ Mac had upregulated pathways related to macrophage activation, interferon-γ response and adipogenesis, including genes such as *IFNGR2, APOD, APOE, MGP,* and *NLRP3,* as well as their previously identified functions (Figures S5A and S5E).[46–48] We compared the gene expression changes of the same cell types between GOs and GDs and identified differentially expressed genes that were downregulated or upregulated (with logFC ≥ 0.5 and adjusted p value <0.05). These were differentially expressed in at least one cell type and uniquely expressed in each cell type of mononuclear phagocytes, as shown in the bottom rectangles (Figure S5D). Inflammation, pro-fibrosis and adipogenesis were indicated through the enrichment of high fold change DEGs in the four clusters (Figure S5C).

To assess the potential transition between CD169⁺ clas_mono and macrophages in orbital tissues, we performed a cellular trajectory analysis using RNA velocity (Figure S6A).[49,50] Our analysis revealed a linear continuum of cellular phenotype that could serve as a differentiation pathway from CD169⁺ clas_mono to CD169⁺ Mac (Figure S6A). Using the CellRank algorithm,[51] we identified lineage drivers along the early (mainly CD169⁺ clas_mono), intermediate, and terminal (mainly CD169⁺ Mac) stages. The cells along this differentiation direction showed dynamic expression of genes related to interferon signaling, myeloid cell differentiation, metabolic process, cell activation, adipogenesis and antigen processing and presentation (Figure S6B). In the early stage, the lineage driver genes included *RETN, OAS1, GSDMD, PSMB8, STAT1,* and *APOBEC3A,* indicating upregulated genes related to interferons and adipogenesis as the latent time progresses; In the intermediate stage, the lineage driver genes included *COX6B1, COX5B,* and *CD74,* suggesting that this stage is involved in higher energy metabolism. In the terminal stage, the lineage driver genes included *CEBPD, IL1B, TNF, NFKB, CCL4, CCL3,* and *JUN,* indicating advanced pro-inflammation and pro-adipogenesis capacity in the cells at this stage.

We further investigated the cell-cell interactions (CCIs) analysis between CD169⁺ Mac and other cells in orbital microenvironment using CellChat. Our results showed that CD169⁺ Mac had more interactive signaling with lipo-fibroblasts (LPFs), myofibroblasts (MYFs), ACKR1⁺ ECs (Endothelial Cells) and pericytes (PCs) in GO compared to other clusters (Figures S7 and S8A). Furthermore, immunofluorescence staining showed an enrichment of PDGFB-PDGFRB and CXCL12-CXCR4 signaling molecules orbital tissues (Figures S8B and S8C). We also identified disruptions in these signaling through a differential expression analysis of ligands and receptors (Figures S8D and S8E).

Taken together, our findings suggest that CD169⁺ clas_mono, a pathopoiesis characteristic cluster in PBMCs of GO, might differentiate into CD169⁺ Mac and retain inflammation-promoting, adipogenesis-promoting, and fibrosis-promoting capability in orbital tissues of GOs.

Circulating monocytes regulate GO development via Cxcl12-Cxcr4 axis

We constructed a GO mouse model and performed validation tests according to a previous research (Figures 5C and S9A–S9C).[52] In the early stage of the GO model, there was an increase in the number of CD169⁺ monocytes infiltrating the orbital tissue as the GO progressed through mass cytometry analysis (Figure 5A). Our CCIs analysis and immunofluorescence staining revealed the upregulation of the Cxcl12-Cxcr4 signaling pathway in orbital tissues with GO, which has been reported to play a pivotal role in MS.[53] Then, we tested the potential impact of the Cxcl12-Cxcr4 axis on the migration of CD169⁺ classical monocytes to orbital tissue (Figure 5B). First, we depleted circulating monocytes in recipient mice through MC21 injection. Next, using small interfering RNA (siRNA), we knocked down Cxcr4 in monocytes isolated from the peripheral blood of GO mouse model and injected these depleted monocytes into recipient mice (Figure 5B). The mass cytometry analysis of orbital tissues showed that the homing of reactive CD169⁺ monocytes to periorbital tissues was hindered after Cxcr4 knockdown in the early GO mouse model (Figure 5B). Concurrently, using small animal MRI, we observed that obstructing peripheral monocytes treated with Cxcr4 siRNA diminished the extent of proptosis (Figure 5C). However, a significantly greater degree of proptosis was observed to recur after injecting CD169⁺ monocytes treated with control siRNA (Figure 5C). These results indicate the significance of Cxcl12-Cxcr4 axis in the recruitment of Cd169⁺ monocytes into orbital tissues.

Expansion of CD169⁺ clas_mono in peripheral blood defines a signature of poor prognosis in GOs

In the clinical samples, we aimed to assess the additional clinical significance of CD169⁺ clas_mono and found that their concentrations were higher in GOs with elevated disease activity levels (determined by Clinical Activity Score) (Figure 5D). This finding highlighted the significant correlation between CD169⁺ clas_mono and disease activity, implying their possible use as clinical markers to distinguish GO in the stage of active inflammation. Additionally, we investigated if CD169⁺ clas_mono could exhibit a reaction to medication in GO. The results showed that

A

B

C

D

E

F

G
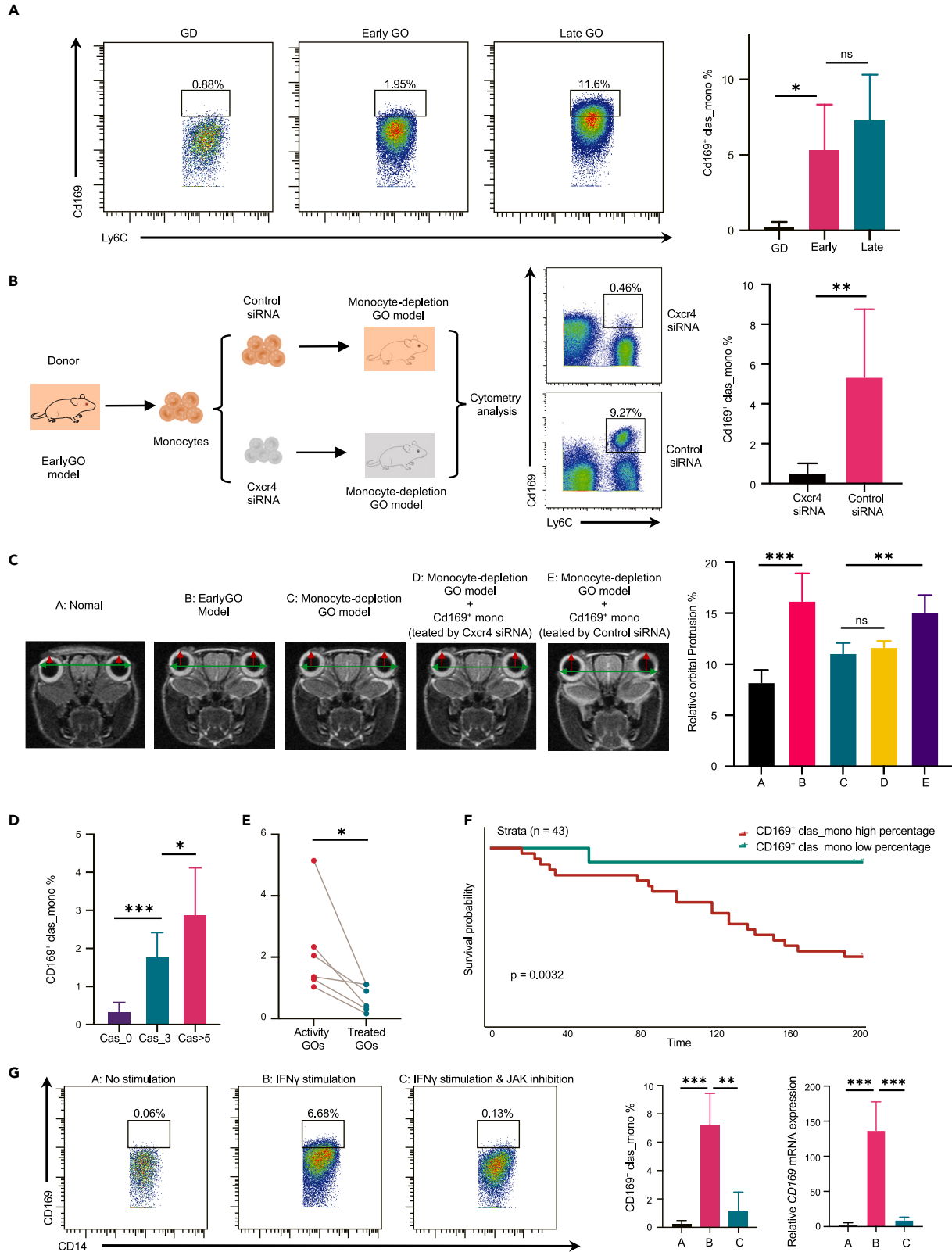
Figure 5. Cd169+ classical monocytes regulate GO development via Cxcl12-Cxcr4 axis

(A) Animal study schema and representative histograms of orbital Cd169+ classical monocytes dynamic proportion in different stages of GO model (n = 5 per stage). All data with error bars are presented as mean ± SD. Statistical analysis was performed using one-way ANOVA. ns, not significant; *p < 0.05.

(B) Monocytes were collected and subjected to *in vitro* siRNA knockdown of Cxcr4. Thereafter, 2 X 10^6 monocytes were i.v. injected into Monocyte-depletion GO model recipient. In the early stage of GO, Monocyte-depletion GO model mice receiving monocytes treated with control siRNA were used as a control. Right histograms represent mass cytometry analysis of orbital Cd169+ classical monocytes exposed to control or Cxcr4 siRNA. n = 6 per group. The data are summarized as the mean ± SD. Statistical analysis was performed using independent-sample t test. **p < 0.01.

(C) MRI images and comparison of orbital protrusion as measured by the distance (indicated by a red arrow) between the highest point of the cornea and the intercanthal line (indicated by a green double arrow) connecting the lateral canthal bony rim of the orbit. All data with error bars are presented as mean ± SD. Statistical analysis was performed using one-way ANOVA. ns, not significant; **p < 0.01; ***p < 0.001.

(D) Proportion of CD169+ clas_mono in circulating monocytes across GOs (n = 28) with different CAS scores. More severe disease states have higher CAS scores. The data are summarized as the mean ± SD. Statistical analysis was performed using one-way ANOVA. *p < 0.05; ***p < 0.001.

(E) Proportion of CD169+ clas_mono in peripheral monocytes from active and immunosuppressant-treated GOs (n = 8). The paired t test was applied.

(F) Survival analysis of GOs stratified by higher and lower CD169+ clas_mono percent.

(G) IFN-γ–stimulated CD169+ clas_mono was decreased after JAK inhibition treatment, detected by qRT-PCR and mass cytometry. All data with error bars are presented as mean ± SD. Statistical analysis was performed using one-way ANOVA. **p < 0.01; ***p < 0.001.

immunosuppressive treatments significantly reduced the number of CD169+ clas_mono in patients after treatment through mass cytometry analysis (Figure 5E) The Janus kinase (JAK)-STAT pathway signaling is a standard mechanism utilized by IFN-γ to activate the activity of STAT1 TF-activity.[54] As we noted activation of STAT1 and IFN-γ signaling in CD169+ clas_mono (Figures 3A and 3B), we then tested the response of CD169+ clas_mono to ruxolitinib (a drug that suppresses JAK-STAT signaling). This drug has recently shown promising results in clinical studies for treating autoimmune diseases and fibrotic lesions.[55–57] Our results showed that ruxolitinib treatment significantly decreased IFN-γ-stimulated CD169+ clas_mono, both in terms of transcriptional and protein levels (Figure 5G). Moreover, we observed a significant improvement in survival analysis among patients with a low proportion of CD169+ classical monocytes (Figure 5F). In conclusion, these findings provided valuable information about the potential of CD169+ clas_mono in evaluating treatment effectiveness and suggested that targeting CD169+ clas_mono may be a promising approach for GO therapy.

DISCUSSION

Our study provides an initial single-cell analysis of the immune environment in peripheral blood from GOs. Using transcriptomic mapping of single cells from circulating blood and orbital tissues of GO patients, we identified specific monocytes that contribute to the hyperinflammatory, fibrotic, and adipogenic nature of GO. Our findings offer potential targets for treatment and clinical assessment. We found that CD169+ clas_mono may have clinical significance in the immunopathogenesis of GO. We observed an expansion of this cell subpopulation in the peripheral blood of patients with elevated disease activity levels, as determined by Clinical Activity Score. In addition, this cell subpopulation was activated by IFN-γ and could be reduced by ruxolitinib. In orbital tissues, our scRNA-seq analysis and validation experiments highlighted the role of CD169+ Mac in inflammation, adipogenesis, and fibrosis.

Monocytes play a crucial role in both innate and adaptive immune responses during infections and contribute to the development of inflammatory diseases through processes such as antigen presentation, phagocytosis, and cytokine secretion.[58] Dysfunctional monocytes have been linked to various autoimmune and autoinflammatory diseases, including atherosclerosis,[59] multiple sclerosis,[60] and rheumatoid arthritis.[61] We grouped monocytes into eight subclusters and discovered that the CD169+ clas_monos from GOs, which were in a terminal state, had an advanced capability in phagocytosis, cytokine secretion, and cell migration compared to GDs. Our analysis showed upregulation of phagocytosis-related genes such as CCL2, CYBA, IL1B, RAB31, SLC11A1, and TNF, cytokine secretion genes like CXCL10, CCL5, IL1B, IRF1, and NLRP3, and cell migration genes like CXCL10, CXCL8, ICAM1, TIMP1, and SELL. CD169, also known as SIGLEC1 and a major marker of macrophage activation, is expressed on tissue resident macrophages and circulating monocytes under inflammatory conditions.[62] Previous studies have shown that CD169 can increase the phagocytic capabilities of monocytes and macrophages,[63] trigger the release of inflammatory cytokines such as TNF-α and IFN-γ, and induce collagen accumulation in monocytes.[61] Consistent with these findings, our experiments showed an expansion of CD169+ clas_mono in the peripheral blood of GO patients, which displayed elevated levels of phagocytosis, migration, and overproduction of proinflammatory cytokines.

The infiltration of monocytes plays a crucial role in the pathology of expanded adipose tissue, where monocyte-derived macrophages collaborate with adipocytes to regulate the inflammatory response.[64,65] The various functions and phenotypes of macrophages have been examined elsewhere in obesity.[46] Our RNA velocity stream analysis in orbital tissues revealed that CD169+ clas_monos preferred to differentiate into CD169+ Macs rather than myeloid-derived DCs, which is consistent with previous reports.[66] CD169+ Macs have been considered regulatory cells that can control excessive pathological adipose tissue inflammation and remodeling in normal mice's white adipose tissues.[65,67] However, our data indicated that CD169+ Macs in GOs underwent pathological changes and lost their normal regulatory functions. Through *in vitro* validation experiments and single-cell transcriptomic analysis, we found that CD169+ Macs expressed upregulated genes and pathways related to pro-inflammation, pro-fibrosis, and pro-adipogenesis. Furthermore, we observed an increase in the number of CD169+ Macs in GOs through immunofluorescence in orbital tissue sections. These results suggest that orbital CD169+ Macs might play a crucial role in recruiting leukocytes into the orbital tissues.

Through our CCIs analysis, we also found that the elevated CXCL12-CXCR4 signaling among CD169+ clas_monos, CD169+ Macs, fibroblasts and ACKR+ ECs. The importance of the CXCL12-CXCR4 pathway in GO was demonstrated by Roshini et al. who focused on CXCL12-CXCR4

and its interactions with TSHR in fibrocytes.[68] The inflammatory and hypoxic environment drove an increase in the number of CD169$^+$ macrophages and CD169$^+$ classical monocytes in orbital tissues through the elevated CXCL12-CXCR4 signaling,[69] forming a vicious circle that exacerbated inflammation, fibrosis, and adipogenesis in the orbital tissues. Additionally, our findings from the GO mouse model indicated that CD169$^+$ clas_mono could exacerbate proptosis degree and migrate into orbital tissues through Cxcr4-Cxcl12 axis. In single-cell PBMC atlas of GO, we noticed the increased expression of Rho–guanosine triphosphatase-related genes (RHOA and RHOB) which played key roles in CXCL12-induced adhesion and motility.[70] Based on these results, we speculated that RHO family might be the main downstream regulator of CXCL12-CXCR4-mediated CD169$^+$ clas_mono migration. We are conducting experiments aimed at attenuating macrophage recruitment and pathological exophthalmos formation in a GO mouse model through RHO inhibition. Given that CXCL12-CXCR4 has been proven to be the major mechanism of various diseases, the pharmaceutical compounds inhibiting CXCL12-CXCR4 may been used as a therapy for GO in the future, such as plerixafor, BL-8040, and ulocuplumab.[71–73]

We observed that STAT1, a vital transcriptional modulator of IFN-γ,[74] was activated through phosphorylation-mediated mechanisms in CD169$^+$ clas_mono in GOs, which is consistent with previous reports of STAT1 activation in CD14$^+$ monocytes and active macrophages in immune diseases.[75,76] Monocytes exposed to elevated IFN signals, particularly high levels of IFN-γ, exhibited an increased level of CD169$^+$ clas_mono, which is consistent with previous observations that exogenous IFNs induced CD169 mRNA synthesis.[77–79] Given that CD4$^+$ T cells are the primary IFN-γ-producing cells, our findings of increased IFN-γ secretion and the fact that CD4$^+$ T cells can enhance CCIs support the hypothesis of activated CD4$^+$ T-driven immunity in GO. Our results suggest that the overactivity of CD4$^+$ T cells in GO patients leads to elevated blood levels of IFN-γ, resulting in the expansion of CD169$^+$ clas_mono. This offers a deeper understanding of the pathogenic effect of CD169$^+$ clas_mono expansion not only in GO but also in various autoimmune diseases.

Clinically, identifying laboratory biomarkers and therapeutic targets for GO is crucial.[1] We found that the expansion of CD169$^+$ clas_mono was associated with GO progression, activity, and prognosis. Furthermore, CD169 protein levels were elevated in GO serum,[80,81] and the presence of CD169$^+$ clas_mono was significantly heightened in several autoimmune diseases. Of significance, CD169$^+$ clas_mono responded positively to ruxolitinib, a highly selective JAK inhibitor that is effective and safe for treating autoimmune diseases and fibrotic lesions.[55–57]

In conclusion, our study provides a detailed depiction of the peripheral immune system in GO at the single-cell level and reveals the changing patterns of different monocyte subtypes. We have demonstrated the involvement of CD169$^+$ clas_mono cells in GO progression. Our findings offer valuable insights into the mechanisms underlying the pathogenesis of GO and provide new directions for further research into its diagnosis, treatment, and prevention.

Limitations of the study

There are several limitations to our study that should be addressed. First, the scarcity of GO cases in the scRNA-seq data may lead to a biased selection, which could affect the validity of our results. To address this issue, we conducted supplementary experiments and analyzed public datasets to validate our findings. Second, while our study focused on the functional phenotypes and markers of CD169$^+$ clas_mono cells, future studies should examine other types of mononuclear phagocytes which may contribute to the development of GO. Importantly, we utilized MC21 to deplete circulating monocytes, such depletion is not CD169 specific. Therefore, further definitive experiments are needed to investigate whether CD169$^+$ monocytes could drive the progression of GO.

STAR★METHODS

Detailed methods are provided in the online version of this paper and include the following:

- KEY RESOURCES TABLE
- RESOURCE AVAILABILITY
  - Lead contact
  - Materials availability
  - Data and code availability
- EXPERIMENTAL MODEL AND STUDY PARTICIPANT DETAILS
  - Human clinical samples
  - GO mouse model
- METHOD DETAILS
  - Single-cell suspensions preparation for peripheral blood and orbital tissues
  - Preparation of scRNA-Seq libraries and sequencing
  - Survival analysis
  - Histological examinations of orbital tissues
  - Immunofluorescence staining
  - Cytokine secretion assay
  - Phagocytosis test
  - Monocyte migration assay
  - IFNs and ruxolitinib stimulation test
  - Enzyme-linked immunosorbent assay (ELISA)

○ RNA extraction and reverse transcription-quantitative PCR (RT-qPCR)
○ Magnetic resonance imaging
○ Flow cytometry
○ Mass cytometry
○ Preparation of mouse orbital tissues
○ Primary cultures of orbital fibroblasts
○ Oil Red O staining
○ Cell co-culture
● QUANTIFICATION AND STATISTICAL ANALYSIS

AUTHOR CONTRIBUTIONS

J.L., D.L.W., and R.Q.T. are jointly responsible for the experimental design, experimental implementation, and manuscript writing. H.S.W., Y.X.Q., X.Y.L., J.S.L., Q.K.Z., and Q.L.H. are responsible for guiding the experimental operation. Z.L., Z.J.L., Y.H.L., and L.S. are responsible for correcting the details of the experimental design. D.Q.W., M.Z., Z.X.S., and W.Y.G. is responsible for collecting sample tissues and conducting primary cell culture. X.C.L. and H.J.Y. are responsible for the overall control of the experiment and revision of the manuscript.

DECLARATION OF INTERESTS

The authors declare no competing interests.

REFERENCES

1. Bahn, R.S. (2010). Graves' ophthalmopathy. N. Engl. J. Med. *362*, 726–738. https://doi.org/10.1056/NEJMra0905750.

2. Smith, T.J., and Hegedüs, L. (2016). Graves' Disease. N. Engl. J. Med. *375*, 1552–1565. https://doi.org/10.1056/NEJMra1510030.

3. Fang, S., Huang, Y., Wang, N., Zhang, S., Zhong, S., Li, Y., Sun, J., Liu, X., Wang, Y., Gu, P., et al. (2019). Insights Into Local Orbital Immunity: Evidence for the Involvement of the Th17 Cell Pathway in Thyroid-Associated Ophthalmopathy. J. Clin. Endocrinol. Metab. *104*, 1697–1711. https://doi.org/10.1210/jc.2018-01626.

4. Antonelli, A., Ferrari, S.M., Fallahi, P., Frascerra, S., Santini, E., Franceschini, S.S., and Ferrannini, E. (2009). Monokine induced by interferon gamma (IFNgamma) (CXCL9) and IFNgamma inducible T-cell alpha-chemoattractant (CXCL11) involvement in Graves' disease and ophthalmopathy: modulation by peroxisome proliferator-activated receptor-gamma agonists. J. Clin. Endocrinol. Metab. *94*, 1803–1809. https://doi.org/10.1210/jc.2008-2450.

5. Hwang, C.J., Afifiyan, N., Sand, D., Naik, V., Said, J., Pollock, S.J., Chen, B., Phipps, R.P., Goldberg, R.A., Smith, T.J., and Douglas, R.S. (2009). Orbital fibroblasts from patients with thyroid-associated ophthalmopathy overexpress CD40: CD154 hyperinduces IL-6, IL-8, and MCP-1. Invest. Ophthalmol. Vis. Sci. *50*, 2262–2268. https://doi.org/10.1167/iovs.08-2328.

6. Wang, Y., Chen, Z., Wang, T., Guo, H., Liu, Y., Dang, N., Hu, S., Wu, L., Zhang, C., Ye, K., and Shi, B. (2021). A novel CD4+ CTL subtype characterized by chemotaxis and inflammation is involved in the pathogenesis of Graves' orbitopathy. Cell. Mol. Immunol. *18*, 735–745. https://doi.org/10.1038/s41423-020-00615-2.

7. Li, Z., Wang, M., Tan, J., Zhu, L., Zeng, P., Chen, X., Xie, L., Duan, R., Chen, B., Tao, T., et al. (2022). Single-cell RNA sequencing depicts the local cell landscape in thyroid-associated ophthalmopathy. Cell Rep. Med. *3*, 100699. https://doi.org/10.1016/j.xcrm.2022.100699.

8. Antonelli, A., Ferrari, S.M., Frascerra, S., Ruffilli, I., Pupilli, C., Bernini, G., Sellari-Franceschini, S., Gelmini, S., Ferrannini, E., and Fallahi, P. (2012). β (CCL2) and α (CXCL10) chemokine modulations by cytokines and peroxisome proliferator-activated receptor-α agonists in Graves' ophthalmopathy. J. Endocrinol. *213*, 183–191. https://doi.org/10.1530/joe-11-0488.

9. Chen, M.H., Chen, M.H., Liao, S.L., Chang, T.C., and Chuang, L.M. (2008). Role of macrophage infiltration in the orbital fat of patients with Graves' ophthalmopathy. Clin.

Endocrinol. *69*, 332–337. https://doi.org/10.1111/j.1365-2265.2008.03219.x.

10. Feldon, S.E., Park, D.J.J., O'Loughlin, C.W., Nguyen, V.T., Landskroner-Eiger, S., Chang, D., Thatcher, T.H., and Phipps, R.P. (2005). Autologous T-lymphocytes stimulate proliferation of orbital fibroblasts derived from patients with Graves' ophthalmopathy. Invest. Ophthalmol. Vis. Sci. *46*, 3913–3921. https://doi.org/10.1167/iovs.05-0605.

11. Narasimhan, P.B., Marcovecchio, P., Hamers, A.A.J., and Hedrick, C.C. (2019). Nonclassical Monocytes in Health and Disease. Annu. Rev. Immunol. *37*, 439–456. https://doi.org/10.1146/annurev-immunol-042617-053119.

12. Smith, T.J., and Hoa, N. (2004). Immunoglobulins from patients with Graves' disease induce hyaluronan synthesis in their orbital fibroblasts through the self-antigen, insulin-like growth factor-I receptor. J. Clin. Endocrinol. Metab. *89*, 5076–5080. https://doi.org/10.1210/jc.2004-0716.

13. Smith, T.J., Padovani-Claudio, D.A., Lu, Y., Raychaudhuri, N., Fernando, R., Atkins, S., Gillespie, E.F., Gianoukakis, A.G., Miller, B.S., Gauger, P.G., et al. (2011). Fibroblasts expressing the thyrotropin receptor overarch thyroid and orbit in Graves' disease. J. Clin. Endocrinol. Metab. *96*, 3827–3837. https://doi.org/10.1210/jc.2011-1249.

14. Kahaly, G.J., Riedl, M., König, J., Pitz, S., Ponto, K., Diana, T., Kampmann, E., Kolbe, E., Eckstein, A., Moeller, L.C., et al. (2018). Mycophenolate plus methylprednisolone versus methylprednisolone alone in active, moderate-to-severe Graves' orbitopathy (MINGO): a randomised, observer-masked, multicentre trial. Lancet Diabetes Endocrinol. 6, 287–298. https://doi.org/10.1016/S2213-8587(18)30020-2.

15. Bartalena, L., Kahaly, G.J., Baldeschi, L., Dayan, C.M., Eckstein, A., Marcocci, C., Marinò, M., Vaidya, B., and Wiersinga, W.M.; EUGOGO † (2021). The 2021 European Group on Graves' orbitopathy (EUGOGO) clinical practice guidelines for the medical management of Graves' orbitopathy. Eur. J. Endocrinol. 185, G43–G67. https://doi.org/10.1530/EJE-21-0479.

16. Leruste, A., Tosello, J., Ramos, R.N., Tauziède-Espariat, A., Brohard, S., Han, Z.Y., Beccaria, K., Andrianteranagna, M., Caudana, P., Nikolic, J., et al. (2019). Clonally Expanded T Cells Reveal Immunogenicity of Rhabdoid Tumors. Cancer Cell 36, 597–612.e8. https://doi.org/10.1016/j.ccell.2019.10.008.

17. Shi, W., Ye, J., Shi, Z., Pan, C., Zhang, Q., Lin, Y., Luo, Y., Su, W., Zheng, Y., and Liu, Y. (2022). Chromatin accessibility analysis reveals regulatory dynamics and therapeutic relevance of Vogt-Koyanagi-Harada disease. Commun. Biol. 5, 506. https://doi.org/10.1038/s42003-022-03430-9.

18. Mao, A.P., Ishizuka, I.E., Kasal, D.N., Mandal, M., and Bendelac, A. (2017). A shared Runx1-bound Zbtb16 enhancer directs innate and innate-like lymphoid lineage development. Nat. Commun. 8, 863. https://doi.org/10.1038/s41467-017-00882-0.

19. Fukui, Y., Hashimoto, O., Sanui, T., Oono, T., Koga, H., Abe, M., Inayoshi, A., Noda, M., Oike, M., Shirai, T., and Sasazuki, T. (2001). Haematopoietic cell-specific CDM family protein DOCK2 is essential for lymphocyte migration. Nature 412, 826–831. https://doi.org/10.1038/35090591.

20. Cimino, P.J., Sokal, I., Leverenz, J., Fukui, Y., and Montine, T.J. (2009). DOCK2 is a microglial specific regulator of central nervous system innate immunity found in normal and Alzheimer's disease brain. Am. J. Pathol. 175, 1622–1630. https://doi.org/10.2353/ajpath.2009.090443.

21. Villarino, A.V., Kanno, Y., and O'Shea, J.J. (2017). Mechanisms and consequences of Jak-STAT signaling in the immune system. Nat. Immunol. 18, 374–384. https://doi.org/10.1038/ni.3691.

22. Wang, Y., Lyu, Y., Tu, K., Xu, Q., Yang, Y., Salman, S., Le, N., Lu, H., Chen, C., Zhu, Y., et al. (2021). Histone citrullination by PADI4 is required for HIF-dependent transcriptional responses to hypoxia and tumor vascularization. Sci. Adv. 7, eabe3771. https://doi.org/10.1126/sciadv.abe3771.

23. Netea, M.G., Lewis, E.C., Azam, T., Joosten, L.A.B., Jaekal, J., Bae, S.Y., Dinarello, C.A., and Kim, S.H. (2008). Interleukin-32 induces the differentiation of monocytes into macrophage-like cells. Proc. Natl. Acad. Sci. USA 105, 3515–3520. https://doi.org/10.1073/pnas.0712381105.

24. Gorabi, A.M., Hajighasemi, S., Kiaie, N., Gheibi Hayat, S.M., Jamialahmadi, T., Johnston, T.P., and Sahebkar, A. (2020). The pivotal role of CD69 in autoimmunity. J. Autoimmun. 111, 102453. https://doi.org/10.1016/j.jaut.2020.102453.

25. Wang, K., Sun, Q., Zhong, X., Zeng, M., Zeng, H., Shi, X., Li, Z., Wang, Y., Zhao, Q., Shao, F., and Ding, J. (2020). Structural Mechanism for GSDMD Targeting by Autoprocessed Caspases in Pyroptosis. Cell 180, 941–955.e20. https://doi.org/10.1016/j.cell.2020.02.002.

26. Zhao, Y., Zhang, Y.D., Zhang, Y.Y., Qian, S.W., Zhang, Z.C., Li, S.F., Guo, L., Liu, Y., Wen, B., Lei, Q.Y., et al. (2014). p300-dependent acetylation of activating transcription factor 5 enhances C/EBPbeta transactivation of C/EBPalpha during 3T3-L1 differentiation. Mol. Cell Biol. 34, 315–324. https://doi.org/10.1128/MCB.00956-13.

27. Gianoukakis, A.G., Khadavi, N., and Smith, T.J. (2008). Cytokines, Graves' disease, and thyroid-associated ophthalmopathy. Thyroid 18, 953–958. https://doi.org/10.1089/thy.2007.0405.

28. Shi, L., Ye, H., Huang, J., Li, Y., Wang, X., Xu, Z., Chen, J., Xiao, W., Chen, R., and Yang, H. (2021). IL-38 Exerts Anti-Inflammatory and Antifibrotic Effects in Thyroid-Associated Ophthalmopathy. J. Clin. Endocrinol. Metab. 106, e3125–e3142. https://doi.org/10.1210/clinem/dgab154.

29. Van de Sande, B., Flerin, C., Davie, K., De Waegeneer, M., Hulselmans, G., Aibar, S., Seurinck, R., Saelens, W., Cannoodt, R., Rouchon, Q., et al. (2020). A scalable SCENIC workflow for single-cell gene regulatory network analysis. Nat. Protoc. 15, 2247–2276. https://doi.org/10.1038/s41596-020-0336-2.

30. Zhou, Y., Zhou, B., Pache, L., Chang, M., Khodabakhshi, A.H., Tanaseichuk, O., Benner, C., and Chanda, S.K. (2019). Metascape provides a biologist-oriented resource for the analysis of systems-level datasets. Nat. Commun. 10, 1523. https://doi.org/10.1038/s41467-019-09234-6.

31. Schroder, K., Hertzog, P.J., Ravasi, T., and Hume, D.A. (2004). Interferon-gamma: an overview of signals, mechanisms and functions. J. Leukoc. Biol. 75, 163–189. https://doi.org/10.1189/jlb.0603252.

32. Sun, Z., Zhong, W., Lu, X., Shi, B., Zhu, Y., Chen, L., Zhang, G., and Zhang, X. (2008). Association of Graves' disease and prevalence of circulating IFN-gamma-producing CD28(-) T cells. J. Clin. Immunol. 28, 464–472. https://doi.org/10.1007/s10875-008-9213-4.

33. Kaufmann, U., Diedrichs-Möhring, M., and Wildner, G. (2012). Dynamics of intraocular IFN-gamma, IL-17 and IL-10-producing cell populations during relapsing and monophasic rat experimental autoimmune uveitis. PLoS One 7, e49008. https://doi.org/10.1371/journal.pone.0049008.

34. Antonelli, A., Rotondi, M., Ferrari, S.M., Fallahi, P., Romagnani, P., Franceschini, S.S., Serio, M., and Ferrannini, E. (2006). Interferon-gamma-inducible alpha-chemokine CXCL10 involvement in Graves' ophthalmopathy: modulation by peroxisome proliferator-activated receptor-gamma agonists. J. Clin. Endocrinol. Metab. 91, 614–620. https://doi.org/10.1210/jc.2005-1689.

35. Jin, S., Guerrero-Juarez, C.F., Zhang, L., Chang, I., Ramos, R., Kuan, C.H., Myung, P., Plikus, M.V., and Nie, Q. (2021). Inference and analysis of cell-cell communication using CellChat. Nat. Commun. 12, 1088. https://doi.org/10.1038/s41467-021-21246-9.

36. Grewal, I.S., and Flavell, R.A. (1996). The role of CD40 ligand in costimulation and T-cell activation. Immunol. Rev. 153, 85–106. https://doi.org/10.1111/j.1600-065x.1996.tb00921.x.

37. McKee, C.M., Penno, M.B., Cowman, M., Burdick, M.D., Strieter, R.M., Bao, C., and Noble, P.W. (1996). Hyaluronan (HA) fragments induce chemokine gene expression in alveolar macrophages The role of HA size and CD44. J. Clin. Invest. 98, 2403–2413. https://doi.org/10.1172/JCI119054.

38. Kuwahara, G., Hashimoto, T., Tsuneki, M., Yamamoto, K., Assi, R., Foster, T.R., Hanisch, J.J., Bai, H., Hu, H., Protack, C.D., et al. (2017). CD44 Promotes Inflammation and Extracellular Matrix Production During Arteriovenous Fistula Maturation. Arterioscler. Thromb. Vasc. Biol. 37, 1147–1156. https://doi.org/10.1161/ATVBAHA.117.309385.

39. Santos, L.L., and Morand, E.F. (2006). The role of macrophage migration inhibitory factor in the inflammatory immune response and rheumatoid arthritis. Wien Med. Wochenschr. 156, 11–18. https://doi.org/10.1007/s10354-005-0243-8.

40. Lang, T., Lee, J.P.W., Elgass, K., Pinar, A.A., Tate, M.D., Aitken, E.H., Fan, H., Creed, S.J., Deen, N.S., Traore, D.A.K., et al. (2018). Macrophage migration inhibitory factor is required for NLRP3 inflammasome activation. Nat. Commun. 9, 2223. https://doi.org/10.1038/s41467-018-04581-2.

41. Sullivan, G.P., O'Connor, H., Henry, C.M., Davidovich, P., Clancy, D.M., Albert, M.L., Cullen, S.P., and Martin, S.J. (2020). TRAIL Receptors Serve as Stress-Associated Molecular Patterns to Promote ER-Stress-Induced Inflammation. Dev. Cell 52, 714–730.e5. https://doi.org/10.1016/j.devcel.2020.01.031.

42. Tamada, K., Shimozaki, K., Chapoval, A.I., Zhai, Y., Su, J., Chen, S.F., Hsieh, S.L., Nagata, S., Ni, J., and Chen, L. (2000). LIGHT, a TNF-like molecule, costimulates T cell proliferation and is required for dendritic cell-mediated allogeneic T cell response. J. Immunol. 164, 4105–4110. https://doi.org/10.4049/jimmunol.164.8.4105.

43. Nehar-Belaid, D., Hong, S., Marches, R., Chen, G., Bolisetty, M., Baisch, J., Walters, L., Punaro, M., Rossi, R.J., Chung, C.H., et al. (2020). Mapping systemic lupus erythematosus heterogeneity at the single-cell level. Nat. Immunol. 21, 1094–1106. https://doi.org/10.1038/s41590-020-0743-0.

44. Zhang, F., Wei, K., Slowikowski, K., Fonseka, C.Y., Rao, D.A., Kelly, S., Goodman, S.M., Tabechian, D., Hughes, L.B., Salomon-Escoto, K., et al. (2019). Defining inflammatory cell states in rheumatoid arthritis joint synovial tissues by integrating single-cell transcriptomics and mass cytometry. Nat. Immunol. 20, 928–942. https://doi.org/10.1038/s41590-019-0378-1.

45. Hong, X., Meng, S., Tang, D., Wang, T., Ding, L., Yu, H., Li, H., Liu, D., Dai, Y., and Yang, M. (2020). Single-Cell RNA Sequencing Reveals the Expansion of Cytotoxic CD4(+) T Lymphocytes and a Landscape of Immune Cells in Primary Sjogren's Syndrome. Front. Immunol. 11, 594658. https://doi.org/10.3389/fimmu.2020.594658.

46. Hill, D.A., Lim, H.W., Kim, Y.H., Ho, W.Y., Foong, Y.H., Nelson, V.L., Nguyen, H.C.B., Chegireddy, K., Kim, J., Habertheuer, A., et al. (2018). Distinct macrophage populations direct inflammatory versus physiological changes in adipose tissue. Proc. Natl. Acad. Sci. USA 115, E5096–E5105. https://doi.org/10.1073/pnas.1802611115.

47. Datta, R., Podolsky, M.J., and Atabai, K. (2018). Fat fibrosis: friend or foe? JCI Insight 3, e122289. https://doi.org/10.1172/jci.insight.122289.

48. Sun, K., Tordjman, J., Clément, K., and Scherer, P.E. (2013). Fibrosis and adipose tissue dysfunction. Cell Metabol. *18*, 470–477. https://doi.org/10.1016/j.cmet.2013.06.016.

49. La Manno, G., Soldatov, R., Zeisel, A., Braun, E., Hochgerner, H., Petukhov, V., Lidschreiber, K., Kastriti, M.E., Lönnerberg, P., Furlan, A., et al. (2018). RNA velocity of single cells. Nature *560*, 494–498. https://doi.org/10.1038/s41586-018-0414-6.

50. Bergen, V., Lange, M., Peidli, S., Wolf, F.A., and Theis, F.J. (2020). Generalizing RNA velocity to transient cell states through dynamical modeling. Nat. Biotechnol. *38*, 1408–1414. https://doi.org/10.1038/s41587-020-0591-3.

51. Lange, M., Bergen, V., Klein, M., Setty, M., Reuter, B., Bakhti, M., Lickert, H., Ansari, M., Schniering, J., Schiller, H.B., et al. (2022). CellRank for directed single-cell fate mapping. Nat. Methods *19*, 159–170. https://doi.org/10.1038/s41592-021-01346-6.

52. Zhang, M., Ding, X., Wu, L.P., He, M.Q., Chen, Z.Y., Shi, B.Y., and Wang, Y. (2021). A Promising Mouse Model of Graves' Orbitopathy Induced by Adenovirus Expressing Thyrotropin Receptor A Subunit. Thyroid *31*, 638–648. https://doi.org/10.1089/thy.2020.0088.

53. Shi, K., Li, H., Chang, T., He, W., Kong, Y., Qi, C., Li, R., Huang, H., Zhu, Z., Zheng, P., et al. (2022). Bone marrow hematopoiesis drives multiple sclerosis progression. Cell *185*, 2234–2247.e17. https://doi.org/10.1016/j.cell.2022.05.020.

54. Hu, X., and Ivashkiv, L.B. (2009). Cross-regulation of signaling pathways by interferon-gamma: implications for immune responses and autoimmune diseases. Immunity *31*, 539–550. https://doi.org/10.1016/j.immuni.2009.09.002.

55. McCoy, S.S., Parker, M., Gurevic, I., Das, R., Pennati, A., and Galipeau, J. (2022). Ruxolitinib inhibits IFNγ-stimulated Sjögren's salivary gland MSC HLA-DR expression and chemokine-dependent T cell migration. Rheumatology *61*, 4207–4218. https://doi.org/10.1093/rheumatology/keac111.

56. Mesa, R.A., Yasothan, U., and Kirkpatrick, P. (2012). Nat. Rev. Drug Discov. *11*, 103–104. https://doi.org/10.1038/nrd3652.

57. Stancil, I.T., Michalski, J.E., Hennessy, C.E., Hatakka, K.L., Yang, I.V., Kurche, J.S., Rincon, M., and Schwartz, D.A. (2022). Interleukin-6-dependent epithelial fluidization initiates fibrotic lung remodeling. Sci. Transl. Med. *14*, eabo5254. https://doi.org/10.1126/scitranslmed.abo5254.

58. Guilliams, M., Mildner, A., and Yona, S. (2018). Developmental and Functional Heterogeneity of Monocytes. Immunity *49*, 595–613. https://doi.org/10.1016/j.immuni.2018.10.005.

59. Jaipersad, A.S., Lip, G.Y.H., Silverman, S., and Shantsila, E. (2014). The role of monocytes in angiogenesis and atherosclerosis. J. Am. Coll. Cardiol. *63*, 1–11. https://doi.org/10.1016/j.jacc.2013.09.019.

60. Dema, M., Eixarch, H., Villar, L.M., Montalban, X., and Espejo, C. (2021). Immunosenescence in multiple sclerosis: the identification of new therapeutic targets. Autoimmun. Rev. *20*, 102893. https://doi.org/10.1016/j.autrev.2021.102893.

61. Xiong, Y.S., Cheng, Y., Lin, Q.S., Wu, A.L., Yu, J., Li, C., Sun, Y., Zhong, R.Q., and Wu, L.J. (2014). Increased expression of Siglec-1 on peripheral blood monocytes and its role in mononuclear cell reactivity to autoantigen in rheumatoid arthritis. Rheumatology *53*, 250–259. https://doi.org/10.1093/rheumatology/ket342.

62. Biesen, R., Demir, C., Barkhudarova, F., Grün, J.R., Steinbrich-Zöllner, M., Backhaus, M., Häupl, T., Rudwaleit, M., Riemekasten, G., Radbruch, A., et al. (2008). Sialic acid-binding Ig-like lectin 1 expression in inflammatory and resident monocytes is a potential biomarker for monitoring disease activity and success of therapy in systemic lupus erythematosus. Arthritis Rheum. *58*, 1136–1145. https://doi.org/10.1002/art.23404.

63. Xiong, Y.S., Wu, A.L., Mu, D., Yu, J., Zeng, P., Sun, Y., and Xiong, J. (2017). Inhibition of siglec-1 by lentivirus mediated small interfering RNA attenuates atherogenesis in apoE-deficient mice. Clin. Immunol. *174*, 32–40. https://doi.org/10.1016/j.clim.2016.11.005.

64. Sun, K., Kusminski, C.M., and Scherer, P.E. (2011). Adipose tissue remodeling and obesity. J. Clin. Invest. *121*, 2094–2101. https://doi.org/10.1172/JCI45887.

65. Xu, X., Grijalva, A., Skowronski, A., van Eijk, M., Serlie, M.J., and Ferrante, A.W., Jr. (2013). Obesity activates a program of lysosomal-dependent lipid metabolism in adipose tissue macrophages independently of classic activation. Cell Metabol. *18*, 816–830. https://doi.org/10.1016/j.cmet.2013.11.001.

66. Asano, K., Takahashi, N., Ushiki, M., Monya, M., Aihara, F., Kuboki, E., Moriyama, S., Iida, M., Kitamura, H., Qiu, C.H., et al. (2015). Intestinal CD169(+) macrophages initiate mucosal inflammation by secreting CCL8 that recruits inflammatory monocytes. Nat. Commun. *6*, 7802. https://doi.org/10.1038/ncomms8802.

67. Chen, Q., Lai, S.M., Xu, S., Tan, Y., Leong, K., Liu, D., Tan, J.C., Naik, R.R., Barron, A.M., Adav, S.S., et al. (2021). Resident macrophages restrain pathological adipose tissue remodeling and protect vascular integrity in obese mice. EMBO Rep. *22*, e52835. https://doi.org/10.15252/embr.202152835.

68. Fernando, R., Atkins, S.J., and Smith, T.J. (2016). Intersection of Chemokine and TSH Receptor Pathways in Human Fibrocytes: Emergence of CXCL-12/CXCR4 Cross Talk Potentially Relevant to Thyroid-Associated Ophthalmopathy. Endocrinology *157*, 3779–3787. https://doi.org/10.1210/en.2016-1382.

69. Ceradini, D.J., Kulkarni, A.R., Callaghan, M.J., Tepper, O.M., Bastidas, N., Kleinman, M.E., Capla, J.M., Galiano, R.D., Levine, J.P., and Gurtner, G.C. (2004). Progenitor cell trafficking is regulated by hypoxic gradients through HIF-1 induction of SDF-1. Nat. Med. *10*, 858–864. https://doi.org/10.1038/nm1075.

70. Bartolomé, R.A., Molina-Ortiz, I., Samaniego, R., Sánchez-Mateos, P., Bustelo, X.R., and Teixidó, J. (2006). Activation of Vav/Rho GTPase signaling by CXCL12 controls membrane-type matrix metalloproteinase-dependent melanoma cell invasion. Cancer Res. *66*, 248–258. https://doi.org/10.1158/0008-5472.Can-05-2489.

71. Bockorny, B., Semenisty, V., Macarulla, T., Borazanci, E., Wolpin, B.M., Stemmer, S.M., Golan, T., Geva, R., Borad, M.J., Pedersen, K.S., et al. (2020). BL-8040, a CXCR4 antagonist, in combination with pembrolizumab and chemotherapy for pancreatic cancer: the COMBAT trial. Nat. Med. *26*, 878–885. https://doi.org/10.1038/s41591-020-0880-x.

72. Wang, J., Tannous, B.A., Poznansky, M.C., and Chen, H. (2020). CXCR4 antagonist AMD3100 (plerixafor): From an impurity to a therapeutic agent. Pharmacol. Res. *159*, 105010. https://doi.org/10.1016/j.phrs.2020.105010.

73. Ghobrial, I.M., Liu, C.J., Redd, R.A., Perez, R.P., Baz, R., Zavidij, O., Sklavenitis-Pistofidis, R., Richardson, P.G., Anderson, K.C., Laubach, J., et al. (2020). A Phase Ib/II Trial of the First-in-Class Anti-CXCR4 Antibody Ulocuplumab in Combination with Lenalidomide or Bortezomib Plus Dexamethasone in Relapsed Multiple Myeloma. Clin. Cancer Res. *26*, 344–353. https://doi.org/10.1158/1078-0432.Ccr-19-0647.

74. Xu, H., Jiang, Y., Xu, X., Su, X., Liu, Y., Ma, Y., Zhao, Y., Shen, Z., Huang, B., and Cao, X. (2019). Inducible degradation of lncRNA Sros1 promotes IFN-gamma-mediated activation of innate immune responses by stabilizing Stat1 mRNA. Nat. Immunol. *20*, 1621–1630. https://doi.org/10.1038/s41590-019-0542-7.

75. Lin, S.H., Chuang, H.Y., Ho, J.C., Lee, C.H., and Hsiao, C.C. (2018). Treatment with TNF-alpha inhibitor rectifies M1 macrophage polarization from blood CD14+ monocytes in patients with psoriasis independent of STAT1 and IRF-1 activation. J. Dermatol. Sci. *91*, 276–284. https://doi.org/10.1016/j.jdermsci.2018.05.009.

76. Hu, X., Herrero, C., Li, W.P., Antoniv, T.T., Falck-Pedersen, E., Koch, A.E., Woods, J.M., Haines, G.K., and Ivashkiv, L.B. (2002). Sensitization of IFN-gamma Jak-STAT signaling during macrophage activation. Nat. Immunol. *3*, 859–866. https://doi.org/10.1038/ni828.

77. Akiyama, H., Ramirez, N.G.P., Gibson, G., Kline, C., Watkins, S., Ambrose, Z., and Gummuluru, S. (2017). Interferon-Inducible CD169/Siglec1 Attenuates Anti-HIV-1 Effects of Alpha Interferon. J. Virol. *91*, e00972-17. https://doi.org/10.1128/JVI.00972-17.

78. Oh, D.S., Oh, J.E., Jung, H.E., and Lee, H.K. (2017). Transient Depletion of CD169+ Cells Contributes to Impaired Early Protection and Effector CD8+ T Cell Recruitment against Mucosal Respiratory Syncytial Virus Infection. Front. Immunol. *8*, 819. https://doi.org/10.3389/fimmu.2017.00819.

79. Kim, H.J., Park, J.H., Kim, H.C., Kim, C.W., Kang, I., and Lee, H.K. (2022). Blood monocyte-derived CD169(+) macrophages contribute to antitumor immunity against glioblastoma. Nat. Commun. *13*, 6211. https://doi.org/10.1038/s41467-022-34001-5.

80. Malhotra, S., Castilló, J., Bustamante, M., Vidal-Jordana, A., Castro, Z., Montalban, X., and Comabella, M. (2013). SIGLEC1 and SIGLEC7 expression in circulating monocytes of patients with multiple sclerosis. Mult. Scler. *19*, 524–531. https://doi.org/10.1177/1352458512458718.

81. Graf, M., von Stuckrad, S.L., Uruha, A., Klotsche, J., Zorn-Pauly, L., Unterwalder, N., Buttgereit, T., Krusche, M., Meisel, C., Burmester, G.R., et al. (2022). SIGLEC1 enables straightforward assessment of type I interferon activity in idiopathic inflammatory myopathies. RMD Open *8*, e001934. https://doi.org/10.1136/rmdopen-2021-001934.

82. Butler, A., Hoffman, P., Smibert, P., Papalexi, E., and Satija, R. (2018). Integrating single-cell transcriptomic data across different conditions, technologies, and species. Nat. Biotechnol. *36*, 411–420. https://doi.org/10.1038/nbt.4096.

83. Eckstein, A.K., Plicht, M., Lax, H., Neuhäuser, M., Mann, K., Lederbogen, S., Heckmann, C., Esser, J., and Morgenthaler,

N.G. (2006). Thyrotropin receptor autoantibodies are independent risk factors for Graves' ophthalmopathy and help to predict severity and outcome of the disease. J. Clin. Endocrinol. Metab. *91*, 3464–3470. https://doi.org/10.1210/jc.2005-2813.

84. Baylis, H.I., Long, J.A., and Groth, M.J. (1989). Transconjunctival lower eyelid blepharoplasty. Technique and complications. Ophthalmology *96*, 1027–1032. https://doi.org/10.1016/s0161-6420(89)32787-4.

85. Wong, C.H., and Mendelson, B. (2017). Extended Transconjunctival Lower Eyelid Blepharoplasty with Release of the Tear Trough Ligament and Fat Redistribution. Plast. Reconstr. Surg. *140*, 273–282. https://doi.org/10.1097/prs.0000000000003561.

86. Secondi, R., Sánchez España, J.C., Castellar Cerpa, J., and Ibáñez Flores, N. (2019). Subconjunctival Orbital Fat Prolapse: An Update on Diagnosis and Management. Semin. Ophthalmol. *34*, 69–73. https://doi.org/10.1080/08820538.2019.1576743.

87. Mehlem, A., Hagberg, C.E., Muhl, L., Eriksson, U., and Falkevall, A. (2013). Imaging of neutral lipids by oil red O for analyzing the metabolic status in health and disease. Nat. Protoc. *8*, 1149–1154. https://doi.org/10.1038/nprot.2013.055.

STAR★METHODS

KEY RESOURCES TABLE

REAGENT or RESOURCE	SOURCE	IDENTIFIER
Antibodies		
Anti-CXCR4 Antibody	Abcam	ab124824
Anti-SDF1 Antibody	Abcam	ab155090
Anti-PDGFB Antibody	Abcam	ab23914
PDGFRB Monoclonal Antibody	Thermo Fisher Scientific	MA5-15143
Anti-IL6 Antibody	Abcam	ab233706
TGF beta-1 Polyclonal Antibody	Thermo Fisher Scientific	PA5-120329
Anti-Apolipoprotein E Antibody	Abcam	ab52607
MARCO Polyclonal Antibody	Thermo Fisher Scientific	PA5-64134
CD169 Monoclonal Antibody	Thermo Fisher Scientific	MA1-16891
Anti-CD14 Antibody	Abcam	ab181470
Purified anti-mouse Ly-6C (Maxpar® Ready) Antibody	Biolegend	128039
Purified anti-mouse CD169 (Siglec-1) Recombinant Antibody	Biolegend	138902
Purified anti-human CD45 (Maxpar® Ready) Antibody	Biolegend	304045
Purified anti-human CD3 (Maxpar® Ready) Antibody	Biolegend	300443
Purified anti-human CD56 (NCAM) (Maxpar® Ready) Antibody	Biolegend	318345
Purified anti-human CD4 Antibody	Biolegend	300502
Purified anti-human CD16 Antibody	Biolegend	302002
Purified anti-human CD14 (Maxpar® Ready) Antibody	Biolegend	301843
Purified anti-human CD169 (Sialoadhesin, Siglec-1) Antibody	Biolegend	346002
PE anti-STAT1 Phospho (Tyr701)	Biolegend	666404
PE anti-human IL-6	Biolegend	501106
Brilliant Violet 421™ anti-human CD169 (Sialoadhesin, Siglec-1)	Biolegend	346018
PE anti-human TNF-α	Biolegend	502909
Biological samples		
Human PBMCs	the First People's Hospital of Zhaoqing	N/A
Human and mouse orbital tissues	Zhongshan Ophthalmic Center	N/A
Chemicals, peptides, and recombinant proteins		
DMEM	Thermo Fisher Scientific	C11330500BT
FBS	Thermo Fisher Scientific	10099141C
Collagenase II	Thermo Fisher Scientific	17101015
PBS	Thermo Fisher Scientific	C10010500BT
DNase I	Sigma-Aldrich	DN25
DAPI	Abcam	ab104139
LPS	Sigma-Aldrich	L2630-10MG
Brefeldin A	Biolegend	420601
Ruxolitinib	Selleck Chemicals	S1378
IFN-α	Abcam	ab48750
IFN-β	MCE	HY-P73128-50ug
IFN-γ	PeproTech	300-02-100

(Continued on next page)

Continued

REAGENT or RESOURCE	SOURCE	IDENTIFIER
Human IFN-α ELISA Kit	Abcam	ab213479
Human IFN-β ELISA Kit	Abcam	ab278127
Human IFN-γ ELISA Kit	Abcam	ab46025
Human IL6 ELISA Kit	Abcam	ab178013
Human TGFB ELISA Kit	Abcam	ab100647
Human APOE ELISA Kit	Abcam	ab108813
Critical commercial assays		
Chromium Single Cell 30 Library & Gel Bead Kit v2	10X Genomics	PN-120237
Deposited data		
scRNA-sequencing data of GO and GD patients	This paper	HRA005673
scRNA-sequencing data of SLE patients	Nehar-Belaid et al.,[43]	GSE135779
scRNA-sequencing data of RA patients	Zhang et al.,[44]	SDY998
scRNA-sequencing data of VKH patients	Shi et al.,[53]	HRA001643
Experimental models: Organisms/strains		
Mouse: BALB/C	the Animal Experimental Center of Zhongshan Ophthalmic Center	N/A
Oligonucleotides		
Human CD169 forward: 5′-GGCTGTTACGATGGTTTATGATGT-3′	This paper	N/A
Human CD169 reverse: 5′-AATCAAAGGCATCATTTTAGGGATA-3′	This paper	N/A
Human GAPDH forward: 5′-GCGAGATCCCTCCAAAATCAA-3′	This paper	N/A
Human GAPDH reverse: 5′-GTTCACACCCATGACGAACAT-3′	This paper	N/A
Software and algorithms		
FlowJo software	FlowJo Co.	N/A
R (version 4.0.0)	R Core	https://www.r-project.org/
Cell Ranger (version 5.0.0)	10x Genomics	https://support.10xgenomics.com/single-cell-gene-expression/software/downloads/latest
Loupe Browser (version 5.0.0)	10x Genomics	https://support.10xgenomics.com/single-cell-gene-expression/software/downloads/latest
velocyto (version 0.12.1)	Van et al.,[29]	https://pyscenic.readthedocs.io/en/latest/
pySCENIC (version 0.17.17)	La et al.,[49]	https://github.com/velocyto-team/velocyto.py
Seurat (version 4.0.0)	Butler et al.,[82]	https://satijalab.org/seurat/
Other		
BD FACSAria II flow cytometer	BD Biosciences	N/A
Digital slide scanner	3DHISTECH	N/A
Magnetic resonance imaging	Bruker	N/A

RESOURCE AVAILABILITY

Lead contact

Further information and requests for resources and reagents should be directed to and will be fulfilled by the lead contact, Xianchai Lin (linxch7@mail.sysu.edu.cn).

Materials availability

This study did not generate new unique reagents.

Data and code availability

- The scRNA-seq datasets analyzed in our article are available from the lead contact upon request under the Genome Sequence Archive in National Genomics Data Center, China National Center for Bioinformation/Beijing Institute of Genomics, Chinese Academy of Sciences (GSA-Human: HRA005673, publicly accessible at: https://ngdc.cncb.ac.cn/gsa-human/browse/HRA005673). The scRNA-seq datasets of SLE, RA, and VKH patients have been deposited at GSE135779 (https://www.ncbi.nlm.nih.gov/geo/query/acc.cgi?acc=GSE135779), SDY998 (https://www.immport.org/shared/study/SDY998), and HRA001643 (https://ngdc.cncb.ac.cn/gsa-human/browse/HRA001643).
- This paper does not report original code.
- Any additional information necessary for reanalyzing the data in this paper is available upon request from the lead contact.

EXPERIMENTAL MODEL AND STUDY PARTICIPANT DETAILS

Human clinical samples

GD diagnosis was based on clinical symptoms of hyperthyroidism, thyroid function test results, and TRAb positivity.[2] GO diagnosis was made by ophthalmologists. Ocular manifestation severity was assessed using the EUGOGO Classification's CAS,[15] the modified NOSPECS,[83] and exophthalmometry at the time of blood sampling.

The orbital tissues from GD patients were obtained only when these patients were also diagnosed with orbital fat prolapse, necessitating lower eyelid blepharoplasty or surgical correction.[84–86] Orbital tissues from GO patients were sourced from surgical remnants following orbital decompression surgery, which was performed after systemic steroid and antithyroid drug treatment.[15]

All experimental procedures were approved by the Ethical Committee of Zhongshan Ophthalmic Center, Sun Yat-Sen University, Guangzhou, China (2016KYPJ028-8). Detailed age and developmental stages of patients in this study are provided in Tables S1, S2, and S3, and all participants were of Han ethnicity. Informed consent was obtained from all patients. The clinical features of all GO and GD patients for all the experiments are listed in Tables S1 and S2.

In addition, we recruited 43 GO patients with CAS ≤ 3 (14 males and 29 females) in Zhongshan Ophthalmic Center (Table S3) and followed them up to determine whether they had an increase in CAS score (i.e. CAS > 3). During the 200-days follow-up, twenty-one patients (48%) had a CAS > 3 and were classified as having poor prognosis (Table S4).

GO mouse model

Experiments used six-week-old female BALB/C mice bred in-house, provided through the Animal Experimental Center of Zhongshan Ophthalmic Center. They were housed in cages with filter-top lids and maintained at 18–22°C on a 12-hour light–dark cycle. The animals were randomly divided into two groups. Twenty-five mice received Ad-TSHRA, and ten mice received the same dose of an adenovirus expressing green fluorescent protein (Ad-EGFP). A prolonged immunization protocol was followed with previous study.[52] After four and seven injections, randomly selected mice challenged with Ad-TSHRA or Ad-EGFP were euthanized for further observations and validations as previously described (Figures S9A–S9C).[52] All procedures of this experiment were approved by the Animal Ethical Committee at Zhongshan Ophthalmic Center, Sun Yat-Sen University.

METHOD DETAILS

Single-cell suspensions preparation for peripheral blood and orbital tissues

To isolate PBMCs, we collected all blood samples from GO or GD patients using Ficoll-Hypaque density solution, which were heparinized and centrifuged for 30 minutes. Single-cell suspensions were then prepared, and cell viability and quantity were determined using Trypan blue staining. For each sample, we ensured that cell viability exceeded 90% before proceeding with experiments. We extracted a fraction of PBMCs for scRNA-seq analysis from each sample containing over 1×10^7 viable cells. Orbital tissues were processed immediately after acquisition, where they were cut into small pieces (<1 mm in diameter) and incubated in DMEM (Thermo Fisher Scientific) containing 2% FBS (Thermo Fisher Scientific), 1 mg/ml collagenase II (Sigma-Aldrich), and 100 mL DNase I (Sigma-Aldrich) for one hour at 37°C on a shaker. The suspension was then diluted with 4 mL DMEM, filtered through a 70-mm cell mesh, and washed with PBS twice. The cell pellet was resuspended in 10 mL of ice-cold red blood cell lysis buffer and incubated at 4°C for 15 minutes. Then, 10 ml of ice-cold PBS was added to the tube and centrifuged at 250g for 10 minutes. After decanting the supernatant, the pellet was resuspended in 5 ml of calcium- and magnesium-free PBS containing 0.04% weight/volume BSA. The single-cell suspension was generated at 700–1200/μl (viability ≥85%) as determined using the Countess II Automated Cell Counter.

Preparation of scRNA-Seq libraries and sequencing

Barcoded single-cell RNA sequencing (scRNA-seq) libraries were prepared using the Chromium Single Cell 3' Reagent v2 kits (10X Genomics), following the manufacturer's protocol. We loaded the single-cell suspensions onto a Chromium Single-Cell Controller instrument (10X Genomics) to produce gel beads in emulsions at the single-cell level. Initially, we performed reverse transcription reactions to produce

barcoded full-length cDNA. This was followed by emulsion disruption using a recovery agent and cDNA clean-up with DynaBeads Myone Silane Beads (Thermo Fisher Scientific). The cDNA was then amplified via polymerase chain reaction, with the cycle number adjusted based on the count of recovered cells (approximately 10,000 cells). The amplified cDNA underwent fragmentation, end-repair, A-tailing and ligation to an index adaptor. Subsequent to this, the library was amplified. Sequencing of each library was carried out on a NovaSeq platform (Illumina), yielding 150 bp paired-end reads. All scRNA-seq datasets were analyzed via using Seurat analysis workflow.[82] We conducted DEGs, Metascape, Pseudo-time trajectory, CCI, pySCENIC, and RNA velocity analyses of scRNA-Seq in accordance with the tutorials provided for each respective software tool. We sourced relevant functional gene sets from the Molecular Signatures Database using specific keywords, such as "PHAGOCYTOSIS", "MIGRATION", "INFLAMMATION", and "CYTOKINE". The scRNA-seq datasets were downloaded from the GEO, ImmPort and National Genomic Data Center (SLE, GSE135779; RA, SDY998; VKH, HRA001643).

Survival analysis

For survival analysis, samples with a CD169+ clas_mono percentage higher than the average were classified into the CD169+ clas_mono high percentage group, while the remaining samples were classified into the CD169+ clas_mono low percentage group. We computed p values using R package survival. Kaplan–Meier curve was plotted using the R package survminer 'ggsurvplot' in R.

Histological examinations of orbital tissues

The mouse orbital tissue was fixed in 4% neutral paraformaldehyde solution, dehydrated, and embedded in paraffin. Subsequently, the whole orbit was sectioned into four coronal slices with 1mm intervals and stained with HE or Masson's trichrome staining method (5 μm thickness). Images were captured using Pannoramic MIDI. The area of retrobulbar adipose tissue (mm^2) in the HE-stained sections was calculated using Adobe Photoshop 2021, with the optic nerve serving as an anatomical landmark. Fibrotic areas in the orbital region appeared blue after Masson's trichrome staining. The luminance tool in Adobe Photoshop 2021 was utilized to analyze the blue pixels in the digital images and calculate the total volume of fibrosis (mm^3) in each retrobulbar region.

Immunofluorescence staining

For immunofluorescence (IF), samples were incubated with primary antibodies and then incubated with secondary antibodies based on the experimental design. The samples were eventually counterstained with DAPI. ImageJ was employed to measure fluorescence intensity. To determine the mean fluorescence intensity for each region in an individual, we first calculated the ratio of the total fluorescence intensity across all visual fields to the total area of these fields in the specified region. This calculation yielded the mean fluorescence intensity for that region. Subsequently, these values were averaged over three randomly selected positions for each individual.

Cytokine secretion assay

Freshly obtained monocytes were resuspended in DMEM and incubated with LPS (20 ng/ml) for 4 h at 37°C and 5% CO_2. After that, surface and intracellular staining was carried out following the methods mentioned earlier. Flow cytometry was employed to determine the ratios of IL-6+ and TNF-α+ cells within the monocyte population. Freshly obtained PBMCs were resuspended in RPMI 1640 and incubated with Cell Activation Cocktail with Brefeldin A (Biolegend) for 5 h at 37°C and 5% CO_2.

Phagocytosis test

To assess phagocytosis ability, freshly isolated monocytes were suspended in 1 ml PBS at a concentration of 5×10^5 cells/ml and then incubated with 1 mg/ml FITC-labeled dextran (70 MW) for 60 minutes. After incubation, the cells were harvested and analyzed using a BD FACSAria II flow cytometer. The difference in mean fluorescence intensity (ΔMFI) between the two conditions (37°C and 4°C) was used to quantify the extent of phagocytosis.

Monocyte migration assay

Transwell 24-well inserts, featuring a 5.0 μm pore size (Permeable Polycarbonate Membrane Inserts, Corning, Fisher Scientific), were coated with collagen G at a concentration of 4 mg/ml (Biochrom). SVEC4-10 endothelial cells (ATCC CRL-2181) were then seeded onto the insert at a density of approximately 1×10^6/ml in 200 μl of DMEM High glucose plus GlutaMAX medium (Gibco, Life Technologies). This medium was supplemented with 10% fetal bovine serum (Gibco, Life Technologies) and 100 U/ml of both penicillin and streptomycin (Sigma-Aldrich). An additional 600 μl of the medium was introduced to the lower wells, and the cells were incubated for 48 hours at 37 °C in a 5% CO2 atmosphere. Following this, the endothelial cells were activated using 10 ng/ml of TNF (PeproTech) for a duration of 4 hours. The medium from both the inserts and wells was then discarded. Subsequently, 600 μl of serum-free RPMI-1640 medium, with ± 80 ng/ml CCL2 (R&D Systems), was added to the wells. Monocytes were introduced to the endothelial-lined inserts at a concentration of 1×10^6/ml in 200 μl of serum-free RPMI-1640 medium. This setup was then incubated for 4 hours at 37 °C in a 5% CO_2 environment.

IFNs and ruxolitinib stimulation test

After preparing single-cell suspensions from blood samples as mentioned above, we utilized the Monocyte Isolation Kit (Miltenyi Biotec) to isolate monocytes, following the manufacturer's instructions. Freshly isolated monocytes were cultured in a 24-well plate containing DMEM at

a density of 5×10^5 cells/ml and stimulated with IFN-α, IFN-β or IFN-γ to activate cellular responses. To evaluate the impact of drug treatment, the cells were incubated for 4 hours in the presence or absence of IFN-γ (10 ng/ml) and 1 μM ruxolitinib (Selleck Chemicals). Subsequently, the cells were harvested at 6 hours, for mRNA detection using PCR and flow cytometry analysis of CD169 expression. The cell culture conditions were maintained at 37°C with 5% CO_2 throughout the duration of the experiment.

Enzyme-linked immunosorbent assay (ELISA)

The serum levels of IFN-α, IFN-β or IFN-γ were measured in triplicate using 96-well half-area plates and a standard plate reader. The assays were performed as per the manufacturer's instructions (Abcam), with appropriate dilutions applied to ensure accuracy.

RNA extraction and reverse transcription-quantitative PCR (RT-qPCR)

Total RNA was prepared from cells monocytes stimulated with IFN-α, IFN-β or IFN-γ for 6 h using an RNA Quick Purification kit (EScience Biotechnology, China). Complementary DNA samples were synthesized with PrimeScript RT Reagent Kit (TaKaRa, China). RT-qPCR was performed on a Roche LightCycler™ 480 by using TB Green Premix Ex Taq II (TaKaRa, China). The primer sequences were as follows: CD169, forward: 5'-GGCTGTTACGATGGTTTATGATGT-3'; reverse: 5'-AATCAAAGGCATCATTTTAGGGATA-3', GAPDH, forward: 5'-GCGA-GATCCCTCCAAAATCAA-3'; reverse: 5'-GTTCACACCCATGACGAACAT-3'. Internal control was Glyceraldehyde phosphate dehydrogenase (GAPDH) and the data were presented as relative gene expression. Each experiment was repeated at least three independent specimens.

Magnetic resonance imaging

In vivo MRI scans were conducted using a horizontal bore 9.4 T MRI scanner (BioSpec 94/30, Bruker, Germany). Throughout the imaging process, mice were anesthetized via inhalation of a 1-2% isoflurane-oxygen mixture. Their heads were positioned within a 25 mm internal diameter quadrature MRI volume coil. We employed a fast spin echo (FSE) sequence to capture T2-weighted MR images, with parameters set as follows: repetition time of 4 s, effective echo time (TE) of 60, echo train length of 8, RARE factor of 16, field of view (FOV) of 26 mm × 26 mm and a matrix size of 256 × 192, resulting in a 100 μm in-plane resolution. We collected four averages of contiguous and coronal slices, each 0.61 mm thick, covering the eyes and a significant portion of the brain. Additionally, twenty-four 0.4 mm thick images with 94 μm in-plane resolution were captured from the eye's surface to its back, aligned perpendicular to the eye's long axis. This orientation mirrors that used in histological processing. The FSE sequence for this had a TR of 1400, effective TE of 7.84, FOV of 12 mm × 12 mm, matrix size of 128 × 128 and 24 averages. Throughout the MRI procedure, we continuously monitored the mice's respiration and temperature, maintaining their body temperature at 37 °C using warm air.

Flow cytometry

Following the preparation of single-cell suspensions from blood samples as described above, we employed the Monocyte Isolation Kit (Miltenyi Biotec) to isolate monocytes, adhering to the manufacturer's guidelines. Then, the cells were fixed and permeabilized following the manufacturer's guidelines and then labeled for TNF-α and IL-6 by incubating them on ice for 50 minutes. For intracellular phosphoprotein staining, the same fixation and permeabilization process was applied, after which the cells were labeled for phospho-STAT1 and incubated on ice for an identical duration. The labeled cells were promptly examined using a BD FACSAria II flow cytometer and analyzed with FlowJo software.

Mass cytometry

Antibodies and reagents

Monoclonal anti-human antibodies for mass cytometry were obtained either pre-conjugated to heavy metal isotopes (Fluidigm, South San Francisco, CA) or conjugated using the MaxPar X8 Chelating Polymer Kit (Fluidigm).

Live cell barcoding and surface staining

We utilized a live cell barcoding methodology to reduce inter-sample staining variability, sample handling time, and antibody consumption. The barcoded and combined samples were stained with 0.5 μmol/l viability dyes (cisplatin-195pt; 201064; Fluidigm), vortexed for 2 minutes at room temperature (RT), and then the reaction was terminated using Maxpar Cell Staining Buffer on a rotating shaker (400 rcf) at RT. The cells were washed and fixed in 1.6% paraformaldehyde in PBS for 10 minutes at RT on a rotary shaker (500 rpm). Next, they were resuspended in pre-cooled Maxpar Cell Staining Buffer to slow the fixation reaction, followed by washing twice with PBS/bovine serum albumin and once with double-distilled water. Finally, the cells were resuspended in a surface antibody mixture and incubated at 37°C for 30 minutes on a rotating shaker (500 rpm) for surface staining. The samples were then stored in freshly diluted 2% formaldehyde in PBS containing 0.125 nmol/l iridium 191/193 intercalator (Fluidigm, 201192) at 4°C overnight.

Preparation of mouse orbital tissues

Orbital tissues from mice were carefully dissected and minced to create a fragmented suspension. This suspension underwent an initial digestion with collagenase II for 80 minutes. Subsequently, a combined digestion with collagenase II (1 mg/ml) and Dispase II (10 U/ml) was performed for an additional 40 minutes. After digestion, the suspension was triturated and rinsed to obtain a mononuclear cell suspension. To improve dissociation, the suspension was passed through a 20-gauge needle syringe several times and then filtered using a 35 mm cell strainer. The final single-cell suspension had a concentration ranging from 700 to 1,200 cells/µl, with a viability of at least 85%, as confirmed by the Countess II Automated Cell Counter.

Primary cultures of orbital fibroblasts

Tissue samples acquired from surgical procedures were finely minced and seeded onto 10 cm culture dishes using high glucose DMEM supplemented with 20% FBS and 1% penicillin/streptomycin. The dishes were then incubated at 37°C with 5% CO_2. Once cells migrated out from the tissue fragments and achieved approximately 90% confluence, they were subcultured using a solution of 0.25% trypsin/EDTA.

Oil Red O staining

We used Oil Red O Staining Kit (Beyotime Biotechnology) and adhered to the provided guidelines: (a) Add the staining wash solution to cover OFs for 20 seconds; (b) Remove the staining wash solution and add Oil Red O (ORO) working solution, stain for 10-20 minutes; (c) Remove the working solution, add the staining wash solution, after 30 seconds, then remove the staining wash solution and wash with PBS for 20 seconds; (d) Add an appropriate amount of PBS to evenly cover OFs. Visualization and quantification of lipid accumulation were conducted in accordance with previously established protocols.[87]

Cell co-culture

After preparing single-cell suspensions from OTs, macrophages were isolated using the CD11b MicroBeads (Miltenyi Biotec) according to the manufacturer's instructions. From these macrophages, CD169^{+} macrophages were further isolated using flow cytometry-based sorting (Figure S5F). Subsequently, CD169^{+} macrophages were seeded in the upper chambers of a 6-well Transwell plate and stimulated with LPS (40 ng/ml). After 24 hours, the medium was replaced with fresh medium and OFs were seeded in the lower chamber. We then placed the upper chambers and lower chambers together. At 48 hours, OFs were subjected to IF staining. To assess the pro-adipogenic capability of CD169^{+} macrophages, we co-cultured LPS-stimulated CD169^{+} macrophages with OFs in pro-adipogenesis medium (DMEM containing 10% fetal bovine serum, 1 µg/ml insulin, 0.25 µg/ml dexamethasone, 30 µg/ml 1-methyl-3-isobutylmethyl-xanthine). After 72 hours, cells were placed in the same medium lacking 1-methyl-3-isobutylmethyl-xanthine (MIX) and dexamethasone. Three days later, OFs were subjected to ORO staining.

QUANTIFICATION AND STATISTICAL ANALYSIS

The data are summarized as the mean $\pm$ SD. Statistical methods have been indicated in the corresponding figures. A two-tailed $p < 0.05$ was considered to indicate statistical significance; *, $p < 0.05$; **, $p < 0.01$; ***, $p < 0.001$; ****, $p < 0.0001$. All statistical analyses were performed using GraphPad Prism v9.0.0 and R v4.0.0.